MIT Open Access Articles

Smoothed particle hydrodynamics and its applications for multiphase flow and reactive transport in porous media

Massachusetts Institute of Technology

Smoothed particle hydrodynamics and its applications for multiphase flow and reactive transport in porous media

A. M. Tartakovsky · N. Trask · K. Pan · B. Jones · W. Pan · J. R. Williams

Abstract Smoothed particle hydrodynamics (SPH) is a Lagrangian method based on a meshless discretization of partial differential equations. In this review, we present SPH discretization of the Navier-Stokes and advection-diffusion-reaction equations, implementation of various boundary conditions, and time integration of the SPH equations, and we discuss applications of the SPH method for modeling pore-scale multiphase flows and reactive transport in porous and fractured media.

Keywords Smoothed particle hydrodynamics · Multiphase flow · Reactive transport · Pore-scale modeling

1 Introduction

In this review, we focus on applications of the smoothed particle hydrodynamics (SPH) method for modeling multiphase flow and reactive transport in porous media at the pore scale. In recent years, pore-scale modeling has become an important part of subsurface science. There is a growing body of evidence that, under certain conditions, existing continuum (Darcy)-scale models do not accurately describe many non-linear processes, including multiphase flows [1] and reactive transport [2]. This realization has given rise to multiscale modeling, which includes pore-scale modeling as an integral part [3, 4]. Pore-scale models also have been used to develop novel effective models [5, 6] and to determine parameters in the existing effective models [6, 7]. Recent advances in numerical methods and increased speed of computers have made direct pore-scale simulations of flow and transport in porous media both possible and practical. A comparative review of numerical methods for pore-scale simulations of flow and transport can be found in [8].

In the SPH method, a computational domain is discretized with a set of points, and a meshless discretization scheme is used to discretize scalar and/or vector fields in terms of their values at these points. The meshless discretization scheme makes it possible to move the discretization points with fluid velocity, even if the velocity field is highly non-uniform. Because of this, SPH can be easily used for solving partial differential equations in a Lagrangian framework, which has a number of benefits for solving the Navier-Stokes (NS) and advection-diffusion equations. In the Lagrangian coordinate system, the absence of the non-linear inertia term in the momentum conservation equation simplifies its solution. For a given velocity field, advection is treated exactly, i.e., there is no numerical dispersion due to discretization of the advective term in the advection-diffusion equation. In SPH, each discretization point has an associated mass and density and can be thought of as the center of a fluid particle. The SPH discretization scheme reduces the NS equations to a system of ordinary

A. M. Tartakovsky (✉) · W. Pan
Pacific Northwest National Laboratory, P.O. Box 999, Richland, WA, 99352, USA
e-mail: alexandre.tartakovsky@pnnl.gov

N. Trask
Brown University, 182 George St, Providence, RI 02906, USA

K. Pan · B. Jones · J. R. Williams
Massachusetts Institute of Technology, Boston, MA, USA

differential equations (ODEs) of Newtonian particle dynamics. The total force acting on any SPH particle is expressed as a sum of the forces acting between this particle and its neighbors. Similar to molecular dynamics, complex fluid-fluid and fluid-solid interactions can be modeled in SPH with pairwise molecular-like interaction forces that are added to the forces obtained from an SPH discretization of the NS equations.

The SPH method was originally developed for modeling highly compressible flows in the context of astrophysical applications [9]. In the SPH model for compressible flows, the particle density (number of discretization points per unit area) changes automatically with fluid density. This provides adaptive resolution as there are always more particles in denser fluid regions where a higher resolution is desired. The SPH method is also well-suited for modeling flows of several fluids as the interface between fluids moves with particles, and there is no need for using complex front tracking schemes. For example, the SPH method has been widely used for modeling breaking waves [10] and ice sheets dynamics [11]. When applied to subsurface flow and transport, the SPH method has been used for modeling unsaturated and multiphase flows, reactive transport, mineral precipitation, and biomass growth. In SPH, incompressible fluid flow can be modeled by solving the compressible NS equations with an appropriate equation of state (the weakly compressible approximation) or the incompressible NS equations. An SPH discretization of the compressible NS equations is straightforward to implement in a scalable parallel computer code, but the timestep for solving the compressible NS equations is limited by the fluid compressibility and is subject to a stiff stability constraint. SPH incompressible flow equations can be integrated with much larger time steps but require a more sophisticated coding. A detailed review of the SPH method and various applications can be found in [9, 12]. In this review, we will focus on the theoretical aspects of SPH that are relevant for hydrogeological modeling, including low-Reynolds number, low-compressible, and incompressible multiphase flows and reactive transport. We will introduce SPH discretization of the NS and advection-diffusion-reaction equations; implementation of Dirichlet, Neumann, and Robin boundary conditions; time integration of the SPH equations; as well as describe various applications of the SPH method for pore-scale modeling of flow and transport in porous media.

2 Governing equations

We consider flow in a porous domain Ω with the sub-domain Ω_P occupied by pores and the sub-domain Ω_S occupied by the solid phase (e.g., soil grains). The flow of the α fluid phase is governed by the NS equations, including the continuity equation

$$\frac{D\rho_\alpha}{Dt} = -\rho_\alpha \left(\nabla \cdot \mathbf{v}_\alpha \right) \quad \mathbf{x} \in \Omega_p \qquad (2.1)$$

and momentum conservation equation

$$\rho_\alpha \frac{D\mathbf{v}_\alpha}{Dt} = -\nabla P_\alpha + \nabla \cdot \boldsymbol{\tau}_\alpha + \rho_\alpha \mathbf{g} \quad \mathbf{x} \in \Omega_p, \qquad (2.2)$$

where $\mathbf{v}_\alpha$ is the velocity vector of the α phase; $\boldsymbol{\tau}_\alpha = \left[\mu_\alpha \left(\nabla \mathbf{v}_\alpha + \nabla \mathbf{v}_\alpha^{\mathrm{T}} \right) \right]$ is the viscous stress tensor; ρ_α is the density; P_α is the pressure; μ_α is the dynamic viscosity; and $\mathbf{g}$ is the gravitational acceleration. Here, $D/Dt = \partial/\partial t + \mathbf{v} \cdot \nabla$ denotes the total derivative. The NS equations are closed with an equation of state

$$P_\alpha = f(\rho_\alpha). \qquad (2.3)$$

At the fluid-fluid interface γ, pressure and velocities satisfy the boundary condition

$$(P_\beta - P_\alpha)\mathbf{n} = (\boldsymbol{\tau}_\beta - \boldsymbol{\tau}_\alpha) \cdot \mathbf{n} + \kappa \sigma \mathbf{n} \quad \mathbf{x} \in \gamma, \qquad (2.4)$$

where $\mathbf{n}$ is the unit normal vector to the interface; subscripts β and α denote the non-wetting and wetting phases, correspondingly; κ is the curvature of the interface; and σ is the constant (in space and time) surface tension. The normal vector $\mathbf{n}$ is assumed to point outward from the non-wetting phase.

The fluid-solid boundary $\Gamma = \Omega_S \cap \Omega_P$ is assumed to be impermeable, resulting in the homogeneous Dirichlet boundary condition for the normal velocity

$$\mathbf{v} \cdot \mathbf{n} = 0 \quad \mathbf{x} \in \Gamma. \qquad (2.5)$$

Here, $\mathbf{n}$ is the unit normal vector to the interface. For the tangential velocity, a well-established boundary condition is the no-slip condition

$$\mathbf{v} \cdot \boldsymbol{m}_1 = 0 \quad \text{and} \quad \mathbf{v} \cdot \boldsymbol{m}_2 = 0 \quad \mathbf{x} \in \Gamma, \qquad (2.6)$$

where $\boldsymbol{m}_1$ and $\boldsymbol{m}_2$ are tangent and bi-tangent unit vectors, correspondingly. At the fluid-fluid-solid contact line $\xi = \Gamma \cap \gamma$, a contact angle θ is imposed. Under static condition, the static contact angle θ_0 can be measured experimentally or determined from the Young condition

$$T_{\alpha\beta} \cos \theta_0 + T_{s\alpha} = T_{s\beta}. \qquad (2.7)$$

Here, T_{ij} is the specific interfacial energy between i and j phases, where subscript s denotes the solid phase and α and β are the two fluid phases. Under dynamic conditions, the contact angle changes depending on the velocity and direction of flow (from the non-wetting to wetting fluid or vice versa). A number of empirical relationships for the dynamic contact angle as a function of the velocity of ξ and the flow direction have been proposed [13, 14]. It should be noted that the no-slip boundary

condition (2.6) at the contact line ξ cannot be satisfied. This, in turn, leads to the well-known singularity in the stress τ at ξ [15]. Approximate models (e.g., creeping flow and lubrication flow [16]) have been proposed for eliminating this singularity.

Solving the multiphase NS equations, especially in geometrically complex domains, can be difficult. As a result, very few grid-based models have been used to model pore-scale multiphase flow in porous media, and they are often limited to flow in small and geometrically simple domains. The Lattice Boltzmann method is a mesoscale method often used to model multiphase flow in porous media and can provide an accurate approximation of the NS equation. A more detailed review of numerical methods for pore-scale multiphase flow and transport can be found in [8].

3 SPH multiphase flow model

3.1 SPH interpolation scheme

In the multiphase SPH model [17], fluid and solid phases are represented by separate sets of particles. These particles serve as discretization points to solve the governing equations. The SPH method is based on a meshless interpolation scheme that allows approximation of a vector or scalar function $\tilde{A}(\mathbf{r}) \approx A(\mathbf{r})$ (e.g., velocity, pressure, density) at position $\mathbf{r}$ in terms of $A(\mathbf{r}_j)$, where $\mathbf{r}_j$ ($j = 1, ..., N$) are the positions of the particles:

$$\tilde{A}(\mathbf{r}) = \int A(\mathbf{r}')W\left(|\mathbf{r} - \mathbf{r}'|, h\right) d\mathbf{r}' \qquad (3.1)$$

and in the discrete form

$$\tilde{\tilde{A}}(\mathbf{r}) = \sum_{j=1}^{N} \frac{A_j}{n_j} W\left(|\mathbf{r} - \mathbf{r}_j|, h\right), \qquad (3.2)$$

where $A_j = A(\mathbf{r}_j)$, N is the total number of SPH particles, $n_j = \rho_j/m_j$ is the particle number density associated with point j, m_j is the mass of particle j, and $\rho_j = \rho(\mathbf{r}_j)$ is the fluid density.

The function W is the SPH smoothing kernel with compact support h ($W(|\mathbf{r}| > h) = 0$). Due to the compactness of W, the summation in Eq. 3.2 can be replaced with the summation over particles within the distance h from $\mathbf{r}$, only. The kernel W must have, at least, a continuous first derivative and satisfy the normalization condition $\int W(\mathbf{r} - \mathbf{r}', h) d\mathbf{r}' = 1$, where integration is performed over the entire domain of A. In the $h \to 0$ limit, W is required

to reduce to the Dirac delta function: $\lim_{h \to 0} W(\mathbf{r} - \mathbf{r}', h) = \delta(\mathbf{r} - \mathbf{r}')$. The number density n_j (the number of SPH particles within volume h^d centered at $\mathbf{r}_j$, where d is the number of spatial dimensions) and h define the resolution of the SPH discretization scheme (3.2).

The total error introduced in Eq. 3.2 can be split between contributions from the integral approximation and the quadrature approximation of the integral with the discrete sum [18],

$$e(\mathbf{r}) = \left\| A(\mathbf{r}) - \tilde{\tilde{A}}(\mathbf{r}) \right\| \leq e(\mathbf{r})_{smoothing} + e(\mathbf{r})_{quadrature}. \qquad (3.3)$$

The first term in Eq. 3.3, $e(\mathbf{r})_{smoothing} = ||A(\mathbf{r}) - \tilde{A}(\mathbf{r})||$, corresponds to smoothing error and is second-order accurate in h. The second term, $e(\mathbf{r})_{quadrature} = ||\tilde{A}(\mathbf{r}) - \tilde{\tilde{A}}(\mathbf{r})||$, scales as $\frac{\Delta}{h}$, where Δ corresponds to a length scale characterizing the average particle separation. To maintain consistency and second-order convergence, both h and $\frac{\Delta}{h}$ should decrease simultaneously. This introduces prohibitive computational cost, and, in practice, $\frac{\Delta}{h}$ (or the number of neighbors) is fixed. To maintain accuracy of the SPH discretization scheme up to practical resolutions, the number of neighbors is commonly set to ≈ 50 for $d = 2$ and 80 for $d = 3$.

3.2 SPH discretization of spatial derivatives

The first derivatives of $\tilde{A}$ and $\tilde{\tilde{A}}$ can be exactly computed by taking derivatives of both sides of Eqs. 3.1 and 3.2, respectively:

$$\nabla_{\mathbf{r}}\tilde{A}(\mathbf{r}) = \int A(\mathbf{r}')\nabla_{\mathbf{r}} W\left(|\mathbf{r} - \mathbf{r}'|, h\right) d\mathbf{r}' \qquad (3.4)$$

and

$$\nabla_{\mathbf{r}}\tilde{\tilde{A}}(\mathbf{r})\big|_{\mathbf{r}=\mathbf{r}_i} = \sum_{j=1}^{N} \frac{A_j}{n_j} \nabla_{\mathbf{r}_i} W\left(r_{ij}, h\right), \qquad (3.5)$$

where $\mathbf{r}_{ij} = \mathbf{r}_i - \mathbf{r}_j$, $r_{ij} = |\mathbf{r}_{ij}|$, and $\nabla_{\mathbf{r}} W\left(|\mathbf{r} - \mathbf{r}_j|, h\right)$ can be found analytically. One of the disadvantages of this discretization scheme is that the derivative of a constant function does not vanish exactly. To ensure that the derivative of a constant is exactly zero, the following renormalization can be used:

$$\nabla A = \frac{1}{\Phi}\left(\nabla(\Phi A) - A\nabla\Phi\right), \qquad (3.6)$$

where Φ is any differentiable function. Applying the discretization (3.4) to both terms on the right-hand side of Eq. 3.6 yields:

$$\nabla_{\mathbf{r}}\tilde{A}(\mathbf{r}) = \frac{1}{\Phi(\mathbf{r})} \int \left(\Phi(\mathbf{r}')A(\mathbf{r}') - A(\mathbf{r})\Phi(\mathbf{r}')\right) \nabla_{\mathbf{r}} W\left(|\mathbf{r} - \mathbf{r}'|, h\right) d\mathbf{r}'. \qquad (3.7)$$

Setting $\Phi(\mathbf{r}) = 1$, we obtain a form of the derivatives, which vanishes exactly for a constant A,

$$\nabla_{\mathbf{r}} \tilde{A}(\mathbf{r}) = \int \left(A(\mathbf{r}') - A(\mathbf{r}) \right) \nabla_{\mathbf{r}} W \left(|\mathbf{r} - \mathbf{r}'|, h \right) d\mathbf{r}', \quad (3.8)$$

or, in discrete form,

$$\nabla_{\mathbf{r}} \tilde{\tilde{A}}(\mathbf{r}) \big|_{\mathbf{r}=\mathbf{r}_i} = \sum_j^N \frac{1}{n_j} \left(A_j - A_i \right) \nabla_{\mathbf{r}_i} W \left(r_{ij}, h \right). \quad (3.9)$$

Alternatively, if we set $\Phi(\mathbf{r}) = \frac{1}{n(\mathbf{r})}$, we obtain an anti-symmetric approximation for the spatial derivative:

$$\frac{1}{n(\mathbf{r})} \nabla_{\mathbf{r}} \tilde{A}(\mathbf{r}) = \int \left(\frac{A(\mathbf{r}')}{n(\mathbf{r}')} + \frac{A(\mathbf{r})}{n(\mathbf{r})^2} n(\mathbf{r}') \right) \nabla_{\mathbf{r}} W \left(|\mathbf{r} - \mathbf{r}'|, h \right) d\mathbf{r}',$$
$$(3.10)$$

and in discrete form,

$$\frac{1}{n_i} \nabla_{\mathbf{r}} \tilde{A}(\mathbf{r}) \big|_{\mathbf{r}=\mathbf{r}_i} = \sum_j^N \left(\frac{A_j}{n_j^2} + \frac{A_i}{n_i^2} \right) \nabla_{\mathbf{r}_i} W \left(r_{ij}, h \right). \quad (3.11)$$

Various forms of SPH discretizations of second derivatives are discussed in [9]. Here, we present an SPH discretization of the divergence of the gradient of a scalar function (or scalar components of a vector or tensor), $\nabla \cdot (k(\mathbf{r}) \nabla A(\mathbf{r}))$, as such terms are present in the momentum and advection-diffusion equations. For a scalar function k, the term $\nabla \cdot (k(\mathbf{r}) \nabla A(\mathbf{r}))$ can be approximated to the second order (in h) in the integral form as

$$\nabla \cdot (k(\mathbf{r}) \nabla \tilde{A}(\mathbf{r})) = \int (k(\mathbf{r}) + k(\mathbf{r}'))(A(\mathbf{r}) - A(\mathbf{r}'))$$
$$\frac{\mathbf{r} - \mathbf{r}'}{|\mathbf{r} - \mathbf{r}'|^2} \cdot \nabla_{\mathbf{r}} W \left(|\mathbf{r} - \mathbf{r}'|, h \right) d\mathbf{r}', (3.12)$$

and in the discrete form as

$$\nabla \cdot \left(k(\mathbf{r}) \nabla \tilde{A}(\mathbf{r}) \right) \big|_{\mathbf{r}=\mathbf{r}_i} = \sum_j^N \frac{k_i + k_j}{n_j} \left(A_i - A_j \right) \frac{\mathbf{r}_{ij}}{r_{ij}^2} \cdot \nabla_{\mathbf{r}_i} W \left(r_{ij}, h \right).$$
$$(3.13)$$

3.3 SPH discretization of Navier-Stokes equations for a single-phase flow

Using the preceding SPH discretization schemes, the momentum conservation Eq. 2.2 can be discretized as:

$$\frac{D\mathbf{r}_i}{Dt} = \mathbf{v}_i, \quad \frac{D(m_i \mathbf{v}_i)}{Dt} = \sum_{j=1}^N \mathbf{f}_{ij} + \mathbf{g} \quad (3.14)$$

$$\mathbf{f}_{ij} = -\left(\frac{P_j}{n_j^2} + \frac{P_i}{n_i^2} \right) \frac{\mathbf{r}_{ij}}{r_{ij}} \frac{dW(r_{ij}, h)}{dr_{ij}} + \frac{4\mu_i \mu_j}{\mu_i + \mu_j} \frac{\mathbf{v}_{ij}}{n_i n_j r_{ij}} \frac{dW(r_{ij}, h)}{dr_{ij}}, \quad (3.15)$$

where $\mathbf{v}_{ij} = \mathbf{v}_i - \mathbf{v}_j$ and, for compactness, we omit the subscript α. In writing Eq. 3.15, we use the equality

$$\nabla_{\mathbf{r}} W(r_{ij}, h) = \frac{\mathbf{r}_{ij}}{r_{ij}} \frac{dW(r_{ij}, h)}{dr_{ij}}. \quad (3.16)$$

The particle density n_i is related to the mass density ρ_i via the expression

$$n_i = \frac{\rho_i}{m_i} \quad (3.17)$$

and is found from the SPH discretization of the continuity equation

$$\frac{Dn_i}{Dt} = n_i \sum_j^N \frac{1}{n_j} \mathbf{v}_{ij} \cdot \nabla_i W(\mathbf{r}_{ij}, h). \quad (3.18)$$

This expression conserves mass only approximately , i.e., the error in mass conservation is on the order of h^2. An alternative approach is to calculate particle density directly from the SPH discretization scheme (3.1) with $A_i = n_i$,

$$n_i = \sum_{j=1}^N W(r_{ij}, h). \quad (3.19)$$

There are two main approaches for incorporating the boundary conditions (2.4) and (2.7): (1) the pair-wise force SPH (PF-SPH) model, which models the surface tension and contact angle using molecular-like pair-wise forces added into the SPH NS equations, and (2) methods based on the continuum surface force (CSF) method [19], where the sharp boundary Γ and contact line γ are approximated with diffused regions and the boundary conditions are replaced with forces acting in these diffused regions. These two methods are described in the following section.

3.4 SPH pair-wise force model for multiphase flows

The boundary conditions (2.4) and (2.7) are the physical consequence of interactions between molecules of different fluid and solid phases. In the PF-SPH model, these boundary conditions are modeled by molecular-like pair-wise interaction forces, $\mathbf{F}_{ij}^{int} = F(r_{ij}) \frac{\mathbf{r}_{ij}}{r_{ij}}$, added in the SPH form of the momentum conservation Eqs. 3.14 and 3.15,

$$\mathbf{f}_{ij} = -\left(\frac{P_j}{n_j^2} + \frac{P_i}{n_i^2} \right) \frac{\mathbf{r}_{ij}}{r_{ij}} \frac{dW(r_{ij}, h)}{dr_{ij}}$$
$$+ \frac{4\mu_i \mu_j}{\mu_i + \mu_j} \frac{\mathbf{v}_{ij}}{n_i n_j r_{ij}} \frac{dW(r_{ij}, h)}{dr_{ij}} - \mathbf{F}_{ij}^{int}. \quad (3.20)$$

As any pair-wise molecular force, the interaction forces $\mathbf{F}_{ij}^{int}$ should be short-range repulsive and long-range attractive. For computational efficiency, the interaction force between two particles is set to zero if the distance between the particles is greater than h. To prevent fluids from mixing and to generate surface tension, the attraction between

particles of the same fluid should be stronger than the attraction between particles of different fluids. Wetting conditions are prescribed by making attraction between particles of the wetting fluid and solid particles stronger than the attraction between particles of nonwetting fluid and solid particles.

The PF-SPH model in the form of Eq. 3.20 was first proposed in [17] with $\mathbf{F}_{ij}^{int}$ given by:

$$\mathbf{F}_{ij}^{int} = \begin{cases} -s_{\alpha\beta}\cos\left(\frac{3\pi}{2h}r_{ij}\right)\frac{\mathbf{r}_{ij}}{r_{ij}} & r_{ij} \leq h \\ 0 & r_{ij} > h, \end{cases} \quad (3.21)$$

where $s_{\alpha\beta}$ is the strength of the interaction force acting between particle i of phase α and particle j of phase β. With such pair-wise forces, the immiscible behavior of the α and β phases is achieved by setting $s_{\alpha\alpha} > s_{\alpha\beta}$ and $s_{\beta\beta} > s_{\alpha\beta}$.

Various forms of $\mathbf{F}_{ij}^{int}$ have been suggested in the literature, including a combination of two SPH weighting functions with different supports h and h_0 ($h > h_0$), $\mathbf{F}_{ij}^{int} = \left[-AW(r_{ij}, h_0) + W(r_{ij}, h)\right]\frac{\mathbf{r}_{ij}}{r_{ij}}$, [20] and $\mathbf{F}_{ij}^{int}$ in the from of the Lennard-Jones force [21]. Prior to the work of [17], Nugent and Posch [22] and Meleán et al. [23, 24] suggested using the van der Waals equation of state (EOS) $P_{vdW} = \frac{k_B T n}{1-an} - bn^2$ (k_B, T, and n are the Boltzmann constant, reference temperature, and number density, respectively, and a and b are the van der Waals parameters) to impose surface tension in free-surface problems and problems concerning liquids in equilibrium with their vapor phases. They demonstrated that the van der Waals EOS in combination with the standard SPH discretization of the pressure gradient term in the momentum conservation equations leads to an equation similar to Eq. 3.20 with $P_i = \frac{k_B T n_i}{1-an_i}$ and purely attractive pair-wise force in the form $\mathbf{F}_{ij}^{int} = -b\frac{\mathbf{r}_{ij}}{r_{ij}}\frac{dW(r_{ij}, h^*)}{dr_{ij}}$. Nugent and Posch reported that to generate a stable interface between liquid and vapor phases, the support h^* of the attractive force should be two times larger than the support h of the viscous and "pressure gradient" forces. One advantage of the PF-SPH formulation (3.20) with a short-range repulsive and long-range attractive force $\mathbf{F}_{ij}^{int}$ is that all forces in the SPH momentum equation can have the same support, which significantly increases the computational efficiency of the method. Another advantage is that this formulation allows a simple treatment of the interfaces between different fluids and different wetting behaviors at the fluid-fluid-solid interfaces.

The interactions between solid-wetting and solid-nonwetting phases are represented by the interaction forces (3.21) with the interaction strengths $s_{s\alpha}$ and $s_{s\beta}$, respectively. The static contact angle is determined by the relative values of $s_{\alpha\alpha}$, $s_{\beta\beta}$, $s_{\alpha\beta}$, $s_{s\alpha}$, and $s_{s\beta}$. For example, for the static contact angle to be less than 90° (the α fluid is a wetting fluid and the β fluid is a non-wetting fluid), the coefficients should satisfy the conditions,

$$s_{s\alpha}/s_{\alpha\alpha} > 1, \quad s_{s\beta}/s_{\beta\beta} < 1. \quad (3.22)$$

To reduce the number of parameters, it is common to set $s_{\alpha\alpha} = s_{\beta\beta}$.

The main advantage of the PF-SPH model is that there is no need to prescribe the dynamic contact angle. Hence, there is no need to rely on approximate or phenomenological models for the dynamic contact angle.

Recently, Bandara et al. [25] demonstrated that the parameters $s_{\alpha\alpha}$, $s_{\beta\beta}$, $s_{\alpha\beta}$, $s_{s\alpha}$, and $s_{s\beta}$ can be related to σ and θ_0 via closed-form analytical expressions based on the theory of surface tension proposed by Young [26], Maxwell [27], and Rayleigh [28].

According to Rayleigh, at equilibrium the surface tension σ between fluids α and β can be found as follows:

$$\sigma = T_{\alpha\alpha} + T_{\beta\beta} - 2T_{\alpha\beta}, \quad (3.23)$$

and the static contact angle between the α and β fluids and the solid phase s is given by Young's Eq. 2.7. In three spatial dimensions, the specific interfacial energy $T_{\alpha\beta}$ can be expressed in terms of the magnitude of the pair-wise forces $m_\alpha m_\beta \phi_{\alpha\beta}(z)$ acting between particles i and j of α and β phases, respectively, and separated by distance z as [27, 28]:

$$T_{\alpha\beta} = \frac{1}{8}\pi\rho_\alpha\rho_\beta\int_0^\infty z^4\phi_{\alpha\beta}(z)dz, \quad (3.24)$$

where thickness of each phase (the dimension in the direction normal to the interface) is larger than the range of interaction of the pair-wise forces. In two spatial dimensions, $T_{\alpha\beta}$ is given by:

$$T_{\alpha\beta} = \frac{1}{3}\rho_\alpha\rho_\beta\int_0^\infty z^3\phi_{\alpha\beta}(z)dz. \quad (3.25)$$

In the following, we present parameterization of the three-dimensional SPH model. The two-dimensional model can be parameterized in a similar way. Under static conditions, the force (3.20) acting between a pair of particles becomes:

$$\mathbf{f}_{ij} = -m_i m_j \phi\left(r_{ij}\right)\frac{\mathbf{r}_{ij}}{r_{ij}}, \quad (3.26)$$

where

$$\phi(z) = \frac{1}{m_i m_j}\left(\frac{p_i}{n_i^2} + \frac{p_j}{n_j^2}\right)\frac{dW(z)}{dz} + \frac{1}{m_i m_j}F(z). \quad (3.27)$$

To simplify analytical derivations of the coefficient of surface tension, we set W to be the Gaussian function,

$$W(z) = \frac{1}{\left(\sqrt{2\pi}\epsilon\right)^d}e^{-\frac{z^2}{2\epsilon^2}}, \quad (3.28)$$

where $\epsilon = h/3$ and d is the number of spatial dimensions. Following Maxwell's assumption of constant mass and number densities within each phase and substituting Eq. 3.27 into Eq. 3.24, we obtain, after integration:

$$T_{\alpha\beta} = -2^{-\frac{d}{2}}\epsilon^{4-d}\pi^{1-\frac{d}{2}}n_\alpha n_\beta \left(\frac{p_\alpha}{n_\alpha^2} + \frac{p_\beta}{n_\beta^2}\right) + \lambda\epsilon^5 n_\alpha n_\beta s_{\alpha\beta},$$
(3.29)

where

$$\lambda = \frac{3}{4\pi^4}\left[2^7 - 3^2 \times 2^4\pi^2 + 3^3\pi^4\right]$$
(3.30)

and n_α and n_β are the number densities in the corresponding fluid phases. Assuming that $n_\alpha = n_\beta$ (i.e., the same resolution is used to discretize both phases), the surface tension between fluids α and β is obtained by combining Eqs. 3.29 and 3.23:

$$\sigma = \lambda\epsilon^5\left(\bar{s}_{\alpha\alpha} + \bar{s}_{\beta\beta} - 2\bar{s}_{\alpha\beta}\right),$$
(3.31)

where

$$\bar{s}_{\alpha\beta} = \rho_\alpha\rho_\beta\frac{s_{\alpha\beta}}{m_\alpha m_\beta} = n_\alpha n_\beta s_{\alpha\beta}.$$
(3.32)

The static contact angle between fluids α and β and the solid phase s is found by combining Eqs. 3.29 and 2.7:

$$\theta = \text{Arccos}\left[\frac{\bar{s}_{\alpha\alpha} - \bar{s}_{\beta\beta} + 2\bar{s}_{s\alpha} - 2\bar{s}_{s\beta}}{\bar{s}_{\alpha\alpha} + \bar{s}_{\beta\beta} - 2\bar{s}_{\alpha\beta}}\right].$$
(3.33)

In the PF-SPH model, three parameters ($\bar{s}_{\alpha\alpha}$, $\bar{s}_{\beta\beta}$, and $\bar{s}_{\alpha\beta}$) define the surface tension between fluids α and β and two additional parameters ($\bar{s}_{s\alpha}$ and $\bar{s}_{s\beta}$) define the static contact angle between fluids α and β and the solid phase s. According to Eqs. 3.31–3.33, an infinite number of combinations of these parameters can result in the same values of the static contact angle and surface tension. To reduce the number of parameters, we set $\bar{s}_{\alpha\alpha} = \bar{s}_{\beta\beta} = 10^\kappa\bar{s}_{\alpha\beta}$. In immiscible flows, the attraction between particles of the same fluid phase is much stronger than the attraction between particles of different phases, which requires $\kappa > 1$. Then, from Eq. 3.31:

$$\bar{s}_{\alpha\alpha} = \bar{s}_{\beta\beta} = \frac{1}{2(1 - 10^{-\kappa})}\epsilon^{-5}\frac{\sigma}{\lambda}$$
(3.34)

and from Eq. 3.33:

$$\bar{s}_{s\alpha} - \bar{s}_{s\beta} = \frac{1}{2}\epsilon^{-5}\frac{\sigma}{\lambda}\cos(\theta).$$
(3.35)

According to Eq. 3.35, θ depends on the difference of $\bar{s}_{s\alpha}$ and $\bar{s}_{s\beta}$. To define $\bar{s}_{s\alpha}$ and $\bar{s}_{s\beta}$ uniquely, we set $\bar{s}_{s\alpha} = \bar{s}_{\alpha\alpha} - \zeta$

and $\bar{s}_{s\beta} = \bar{s}_{\alpha\alpha} + \zeta$. Substituting this into Eq. 3.35 yields the final expression for $\bar{s}_{s\alpha}$ and $\bar{s}_{s\beta}$:

$$\bar{s}_{s\alpha} = \frac{1}{2}\epsilon^{-5}\frac{\sigma}{\lambda}\left(\frac{1}{1 - 10^{-\kappa}} + \frac{1}{2}\cos\theta\right) \quad \text{and}$$

$$\bar{s}_{s\beta} = \frac{1}{2}\epsilon^{-5}\frac{\sigma}{\lambda}\left(\frac{1}{1 - 10^{-\kappa}} - \frac{1}{2}\cos\theta\right).$$
(3.36)

For sufficiently large κ (in SPH simulations $\kappa = 4$ is usually used), Eqs. 3.34 and 3.36 are reduced to

$$s_{\alpha\alpha} = s_{\beta\beta} = \frac{1}{2}n^{-2}\left(\frac{h}{3}\right)^{-5}\frac{\sigma}{\lambda}$$
(3.37)

and

$$s_{s\alpha} = \frac{1}{2}n^{-2}\left(\frac{h}{3}\right)^{-5}\frac{\sigma}{\lambda}\left(1 + \frac{1}{2}\cos\theta\right) \quad \text{and}$$

$$s_{s\beta} = \frac{1}{2}n^{-2}\left(\frac{h}{3}\right)^{-5}\frac{\sigma}{\lambda}\left(1 - \frac{1}{2}\cos\theta\right),$$
(3.38)

where $n = n_\alpha = n_\beta$ is the average particle number density. Equations 3.37 and 3.38 express the parameters $s_{\alpha\beta}$ in the PF-SPH model as functions of the surface tension, static contact angle, and the SPH discretization parameters n and h. The preceding analysis can be easily extended for other forms of $\mathbf{F}_{ij}^{int}$.

3.5 SPH multiphase models based on the continuum surface force model

Another approach to modeling surface tension is based on the continuum surface force model (CSF) [19]. According to the CSF model, the momentum conservation Eq. 2.2 subject to the boundary condition (2.4) can be rewritten as:

$$\rho\frac{D\mathbf{v}}{Dt} = -\nabla P + \nabla \cdot \boldsymbol{\tau} + \rho\mathbf{g} + \mathbf{F} \quad \mathbf{x} \in \Omega.$$
(3.39)

Assuming that the fluid is inviscid, the surface force $\mathbf{F}$ can be expressed in terms of the surface tension as:

$$\mathbf{F} = \sigma\kappa\nabla\psi,$$
(3.40)

where ψ is the color function

$$\psi(\mathbf{x}) = \begin{cases} 1, & \mathbf{x} \in \Omega_\beta, \\ 0, & \mathbf{x} \in \Omega_\alpha, \end{cases}$$
(3.41)

where Ω_β and Ω_α are the domains occupied by β and α fluid phases, respectively.

The curvature κ can be found as:

$$\kappa = \nabla \cdot \mathbf{n}$$
(3.42)

and the normal unit vector can be calculated using ψ as:

$$\mathbf{n}(\mathbf{x}) = \frac{\nabla\tilde{\psi}(\mathbf{x})}{|\nabla\tilde{\psi}(\mathbf{x})|}, \quad \mathbf{x} \in \Omega.$$
(3.43)

The gradient of ψ is defined according to the SPH integral approximation of derivatives (3.8),

$$\nabla_{\mathbf{r}} \tilde{\psi}(\mathbf{r}) = \int \left(\psi(\mathbf{r}') - \psi(\mathbf{r}) \right) \nabla_{\mathbf{r}} W \left(|\mathbf{r} - \mathbf{r}'|, h \right) d\mathbf{r}'. \quad (3.44)$$

The direct SPH discretization of the Eqs. 3.39–3.43 was found to produce noisy estimates of κ and non-physical negative pressures [29]. In [30], it was shown that the CSF-SPH model can be improved by computing $\nabla \tilde{\psi}$ in Eq. 3.44 using the SPH expression (3.11). In [30], the SPH-CSF model was also extended for modeling three-phase flow and fluid-fluid-solid contact line dynamics. A number of other modifications to CSF-based SPH models have been recently proposed. One of the challenges in CSF-based SPH models is that they require a relatively high numerical resolution to obtain noise-free estimations of the normal and/or curvature in the force $\mathbf{F}$. Because of this, to date, these SPH models have been mostly used for flow simulations in domains such as a single channel or pore with a simple geometry, i.e., in simulations that can afford sufficient numerical resolution.

3.6 Error analysis of SPH derivative operators and operator corrections

The truncation errors of the SPH discretization of spatial derivatives have been studied numerically in [31, 32] and analytically in [18, 33]. In SPH, particles move with the fluid velocity and become disordered in the nonuniform velocity field. In addition to the errors defined in Eq. 3.3, the differential SPH operators are sensitive to an error $||e_{anisotropy}||$ due to the irregularity of the particle configuration. Hence, the total error in the SPH discretization of spatial derivatives is:

$$||e|| \leq ||e_{smoothing}|| + ||e_{quadrature}|| + ||e_{anisotropy}||. \quad (3.45)$$

The scaling of the first two error terms with h and Δx is discussed in Section 3.1. The anisotropy error is zero for a Cartesian grid of particles. For irregularly distributed particles, it scales as:

$$||e_{anisotropy}|| \leq C \frac{\chi}{h^p} \left(\frac{\Delta x}{h} \right)^{\beta}, \quad (3.46)$$

where χ is a length scale characterizing the magnitude of perturbation of the particle arrangement from a Cartesian grid, p denotes the order of the differential operator, and β is an integer corresponding to the order of kernel used in the approximation. A detailed error analysis of the different differential operators can be found in the recent work by Fatehi and Manzari [33].

To demonstrate the effect of irregular particle distribution on the accuracy of SPH discretization of spatial

derivatives, we compute the gradient and Laplacian of the function $u(x, y) = sin(x)sin(y)$ in a periodic two-dimensional domain discretized with randomly distributed SPH particles. The particle positions are obtained by placing the particles on a Cartesian grid with grid spacing Δx and perturbing the positions of particles by a uniformly distributed variable scaled by χ. Figure 1 demonstrates the behavior of the error in approximating the gradient and Laplacian of $u(x, y)$ for increasing values of χ and fixed $\frac{h}{3\Delta x} = 1.5$ using the SPH discretizations (3.11) and (3.13). For moderately perturbed particle arrangements typical of those found in SPH low-Reynolds-number flow simulations, it is possible to achieve 1 % error in the approximation of the gradient. However, for the Laplacian operator, after reaching a value of O(1 %), the error diverges with increasing resolution as the $e_{anisotropy}$ error dominates. It is possible to control $e_{anisotropy}$ by increasing the number of neighbors per particle, i.e., decreasing $\frac{\Delta x}{h}$ at the cost of a significant increase in the total number of SPH particles.

The SPH method's accuracy can be further improved by using SPH discretizations of spatial derivatives that enforce exact approximation of the first and second derivatives of a linear function (i.e., the first derivative of a linear function is a constant, and the second derivative of a linear function is zero) [33]. This requires the construction of small correction tensors for each SPH particle. While this increases the computational complexity of the method and makes resulting schemes non-conservative, it is possible to do this without affecting the method's scalability. Figure 2 demonstrates the behavior of the truncation error and effect of particle disorder as a function of the number of particles when the correction tensors are applied to compute first and second derivatives of u. Comparing Figs. 1 and 2 shows that the correction tensors can reduce the number of particles while maintaining a relatively small total error.

While these corrected operators preserve convergence rate and consistency, they sacrifice the method's conservation properties. More research is needed to determine what approach will be best for low Reynolds number multiphase flows. Hashemi et al. [34] recently used the corrected operators to study the settling of rigid particles in a viscous fluid with encouraging results.

4 Incompressible and low-compressible SPH approximations

In most hydrogeological and petroleum applications, the flow can be characterized by a very low Mach number (i.e., $Ma = \frac{c}{v} \ll 1$). Under this condition, fluids are modeled as incompressible with a corresponding solenoidal velocity field $\nabla \cdot \tilde{v} = 0$. In SPH, this divergence-free constraint

Fig. 1 L^2 norm of truncation error for gradient (panel **a**) and Laplacian (panel **b**) operators applied to the function $u(x, y) = sin(x)sin(y)$ with fixed $\frac{h}{3\Delta x} = 1.5$. While particles on a Cartesian lattice give second-order convergence due to symmetry, as particle positions are shifted by increasingly large random perturbations, the truncation error grows
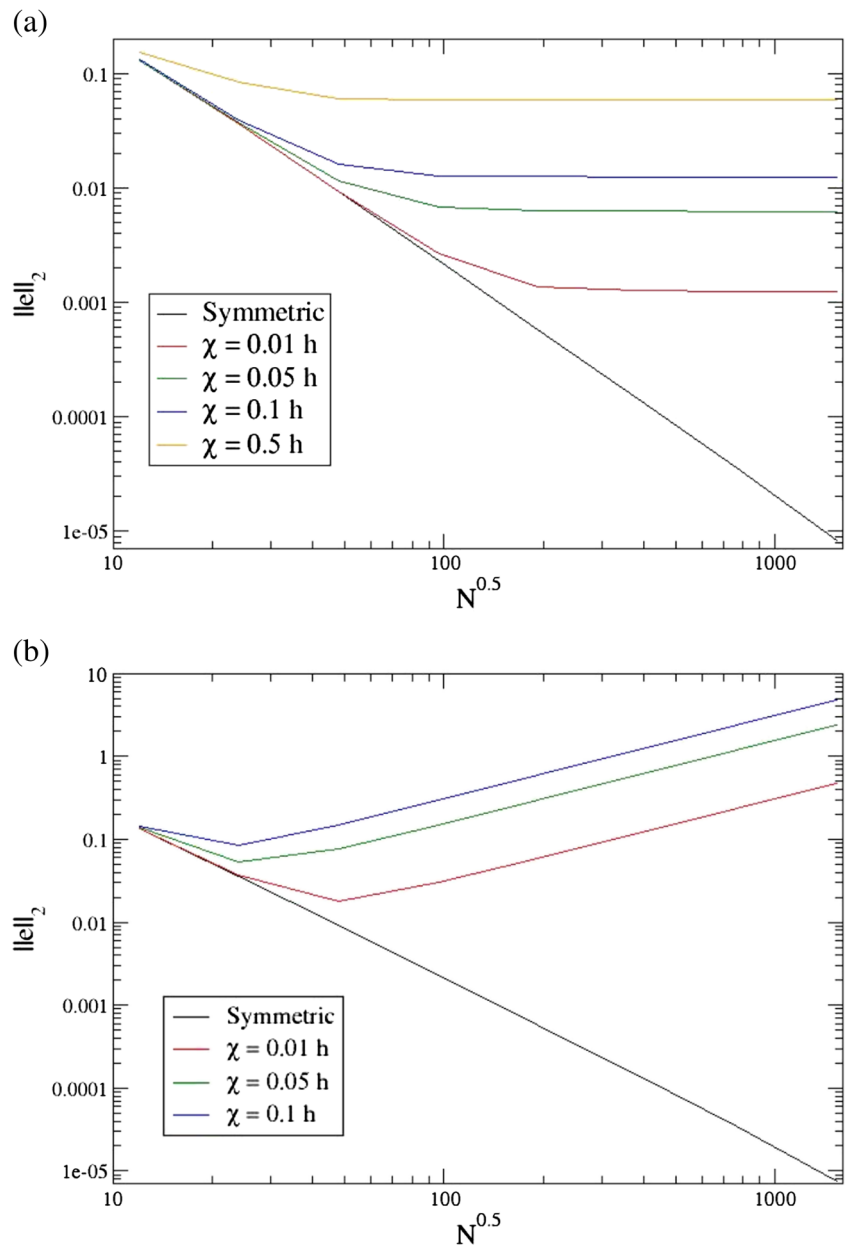
is enforced either by applying a penalty term to density variations in the so-called "weakly compressible" SPH formulation (WCSPH) or by using the incompressible SPH (ISPH) method, which relies on a projection approach.

In the WCSPH formulation, an artificial EOS

$$P = f(\rho) \tag{4.1}$$

is imposed with a sound speed $c = \sqrt{\frac{\partial P}{\partial \rho}}$, selected large enough to control density fluctuations but small enough to avoid a stiff stability restriction on the timestep. A similar approach also has been used in grid-based methods for

incompressible flows [35, 36]. Various EOS have been proposed in the SPH literature, including the ideal gas EOS [37]

$$P = \frac{P_0}{\rho_0}\rho, \tag{4.2}$$

and the non-linear EOS [38]

$$P = P_0\left[(\rho/\rho_0)^\zeta - 1\right]. \tag{4.3}$$

In these EOS, ρ_0 and P_0 are the reference density and pressure, and the exponent ζ is commonly set to 7 for liquids and 1 for gases. To limit the relative density fluctuation to approximately 1 %, the speed of sound should be set to

Fig. 2 L^2 norm of truncation error for the renormalized gradient (panel **a**) and Laplacian (panel **b**) operators updated with the correction tensors [33] and applied to the function $u(x, y) = sin(x)sin(y)$ with fixed $\frac{h}{3\Delta x} = 1.5$. Convergence to the exact result is sustained with increased resolution, and increasing particle disorder results in a transition from second- to first-order convergence at fine resolutions. The renormalized gradient and Laplacian operators are obtained according to [33]
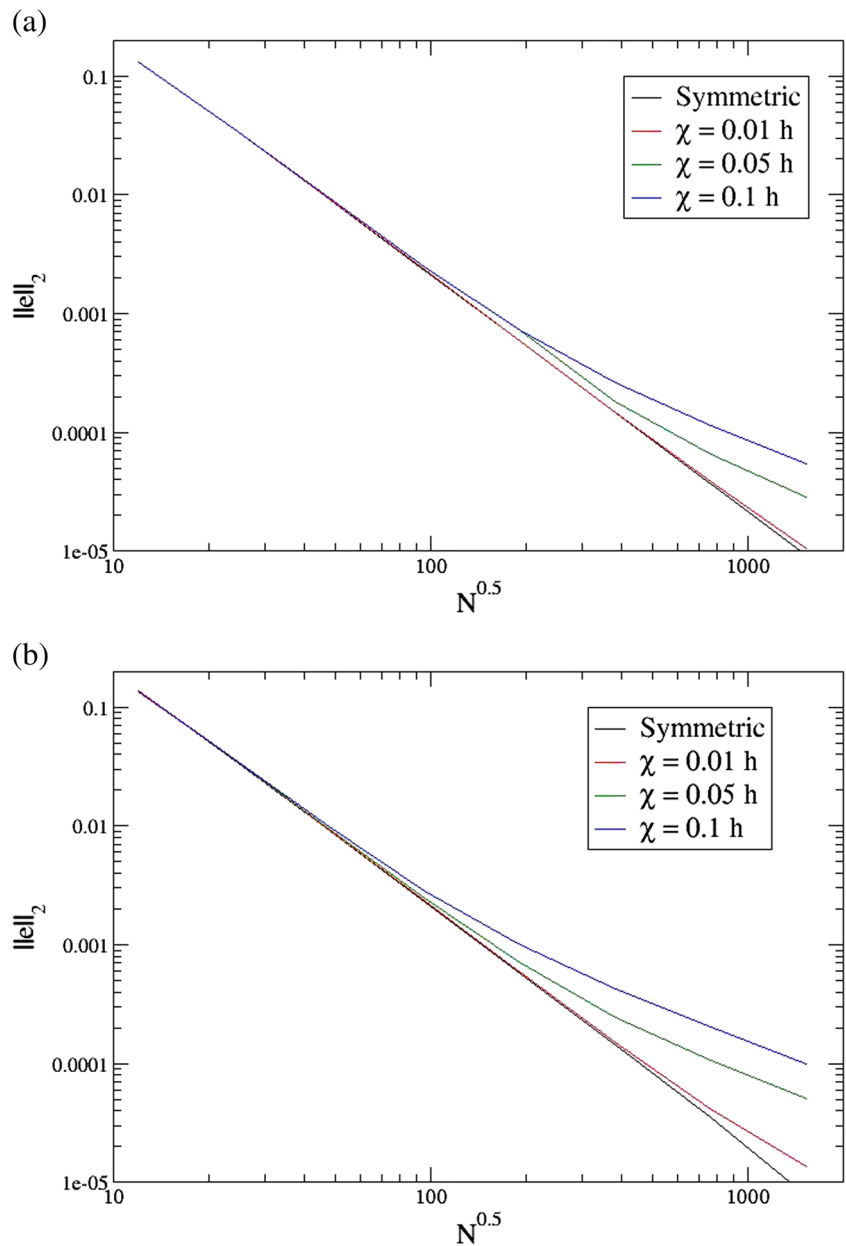
$c = 10V_{\max}$, where $V_{\max}$ is the estimated maximum velocity in a given simulation. Under such conditions, a slightly compressible fluid behaves like the incompressible fluid. For many applications, modeling elliptic incompressible equations with a hyperbolic compressible system requires using either proper non-reflecting boundary conditions [39] or numerical stabilization [10] to control the influence of the corresponding numerical acoustic modes. It can be demonstrated that applying the weakly compressible formulation is equivalent to solving the alternative problem

$$\frac{d\mathbf{v}}{dt} = -\frac{1}{\rho}\nabla p + \frac{\mu}{\rho}\nabla^2\mathbf{v}, \tag{4.4}$$

$$\frac{dp}{dt} + \rho c^2 \nabla \cdot \mathbf{v} = 0, \tag{4.5}$$

which is consistent with the incompressible NS equations only for steady flows or for large c^2. Many authors neglect to acknowledge the resulting consequence: when simulating transient flows using the WCSPH formulation, the sensitivity of the results to the artificial sound speed must be investigated.

The EOS (4.3) with $\zeta = 7$ produces small density variations even for flows with high Reynolds numbers. Coversely, with this EOS, even small errors in density are amplified into large errors in pressure and may result in spurious pressure fluctuations. For low-Reynolds-number flow SPH simulations, the EOS (4.3) with $\zeta = 1$ has been shown to produce both small density variations and smooth density profiles [35–37]. The subtraction of 1 in the EOS

(4.3) was originally proposed for SPH free-surface models to avoid a pressure jump near the free surface. The main disadvantage of this approach is that for $\rho_i < \rho_0$, the resulting pressure gradient force in the SPH momentum equation becomes purely attractive, which was shown to lead to so-called "tensile instability" [40, 41]. For low-Reynolds-number flows with SPH particles occupying the entire computational domain, some authors reported that better SPH results (in terms of the accuracy of pressure and density and the stability of the simulations) are obtained using EOS (4.2) (e.g., [37, 42]), while others have successfully used the $P = P_0[(\rho/\rho_0) - 1]$ EOS (e.g., [43]).

In the alternative ISPH formulation, projection methods are used to solve the incompressible NS equations [44–46]. Typically, a predictor velocity field $\mathbf{v}^*$ is determined by treating the viscous term explicitly:

$$\frac{\mathbf{v}^* - \mathbf{v}^n}{\Delta t} = \frac{\mu}{\rho}\nabla^2 \mathbf{v}^n \qquad (4.6)$$

or alternatively by treating the viscous term implicitly and solving a Helmholtz problem:

$$\frac{\mathbf{v}^* - \mathbf{v}^n}{\Delta t} = \frac{\mu}{\rho}\nabla^2 \mathbf{v}^*. \qquad (4.7)$$

The second approach is standard in mesh-based methods, and has been discussed in the context of a variety of SPH schemes [47, 48].

As Eq. 4.7 is implicit and requires the solution of a system of linear equations, many authors opt to solve instead Eq. 4.6, which treats the viscous term explicitly. However, we note that in the matrix resulting from Eq. 4.7, the off-diagonal terms are dominant as they are scaled by $\Delta t\mu/\rho$. Therefore, this matrix is well-conditioned. Because of this, iterative methods for solving the resulting system of linear equations converge quickly, and there is little to be gained by treating the viscous term explicitly, as this imposes a stiff viscous timestep restriction. Following the predictor step, a pressure gradient is imposed to ensure that the velocity at the end of the timestep is divergence-free:

$$\frac{\mathbf{v}^{n+1} - \mathbf{v}^*}{\Delta t} = -\frac{1}{\rho}\nabla p^{n+1}. \qquad (4.8)$$

Taking the divergence of this equation and requiring that $\nabla \cdot \mathbf{v}^{n+1} = 0$ yields a Poisson problem for the pressure:

$$\nabla^2 p^{n+1} = \frac{\nabla \cdot \rho\mathbf{v}^*}{\Delta t}. \qquad (4.9)$$

Solving this Poisson problem for the pressure yields a velocity at the end of the timestep that is divergence-free up to the truncation error of the Laplacian operator. In Eqs. 4.8 and 4.9, the density is assumed constant within a given

phase, and appropriate Dirichlet and Neumann boundary conditions must be applied for the velocity and pressure, respectively. While the need to solve two linear systems in this method imposes a substantial increase in computational complexity, using implicit schemes allows the use of larger timesteps, which can offset the additional computational overhead. This is particularly relevant to low Reynolds number flows for which explicit schemes are restricted by a viscous constraint on the timestep size of the form $\frac{\mu\Delta t}{\rho h^2} \leq 1$, but the implicit projection methods are restricted only by the Courant-Friedrichs-Lewy (CFL) condition $\frac{V_{max}\Delta t}{h} \leq 1$. Therefore, the number of timesteps required by an explicit method N_{WCSPH} compared to the implicit method N_{ISPH} scales like $\frac{N_{WCSPH}}{N_{ISPH}} \sim \frac{\nu}{V_{max}h}$, or as the inverse of the particle Reynolds number. Numerical experiments confirm that for small Reynolds number flows, the total central processing unit, or CPU, time for each method scales as $\frac{T_{WCSPH}}{T_{ISPH}} \sim \frac{1}{h}$, resulting in a typical order of magnitude speedup in ISPH relative to WCSPH [49].

At present, WCSPH is the most commonly used SPH method in the literature. Due to the fully explicit nature of the method, WCSPH is simple to code and easily parallelizable (simulations have been performed for systems consisting of billions of particles [50]).

While projection methods have been standard in classical Eulerian methods for some time, ISPH has only achieved popularity recently in the SPH community since its initial formulation in 1999 by Cummins and Rudman [44]. The additional complexity of the linear solvers makes for a more challenging framework to work with, and it is no longer possible to use existing particle-particle libraries to implement the method. In comparison to grid-based methods, the resulting linear systems found in ISPH are significantly less sparse and, therefore, more challenging to solve using iterative methods. Maintaining scalability while solving these systems is a challenge and requires efficient preconditioners, such as algebraic multigrid to simulate large 3D systems.

The advances of fast preconditioning libraries, however, promise to resolve these issues, and it is anticipated that ISPH methods will play a more dominant role in the future due to their ability to simulate viscous dynamics efficiently and without introducing artificial acoustic effects. Recently, incompressible SPH simulations have been demonstrated to scale for up to 100 million particles using algebraic multigrid to handle the resulting linear systems [49].

5 Time integration

Due to the explicit form of the WCSPH discretization, standard multistage (e.g., Runga-Kutta) or multilevel (e.g., Adams-Bashforth) explicit timestepping schemes may be

used to simultaneously advance particle positions and velocities forward in time. Alternatively, various simple-to-implement second-order schemes, popular in Molecular Dynamics, also can be used in SPH. The choice of time integration algorithm also depends on which density computation scheme, Eqs. 3.18 or 3.19, is used. For example, Tartakovsky et al. [20, 51, 52] used the "velocity Verlet" timestepping algorithm [53] to integrate the SPH momentum equation with density found from Eq. 3.19:

$$\mathbf{r}_i(t + \triangle t) = \mathbf{r}_i(t) + \triangle t \mathbf{v}_i(t) + \frac{\triangle t^2}{2m_i}\mathbf{f}_i(t) \qquad (5.1)$$

$$\mathbf{v}_i(t + \triangle t) = \mathbf{v}_i(t) + \frac{\triangle t}{2m_i}\left[\mathbf{f}_i(t) + \mathbf{f}_i(t + \triangle t)\right]. \qquad (5.2)$$

At each time step, the density is evaluated using Eq. 3.19, the pressure is obtained from the EOS (4.2) or (4.3) (or any other appropriate EOS), and the force is calculated from the momentum conservation Eq. 3.14.

The advantage of using Eq. 3.19 for density evaluation is that in an infinite or periodic domain Ω, this equation produces density approximations that conserve mass exactly. To see this, rewrite Eq. 3.19 as $\rho(\mathbf{x}) = \sum_j m_j W(\mathbf{x} - \mathbf{x}_j)$ and integrate over Ω to obtain $\int_\Omega \rho(\mathbf{x})d\mathbf{x} = \int_\Omega \sum_j m_j W(\mathbf{x} - \mathbf{x}_j)d\mathbf{x} = \sum_j m_j$. However, for free-surface flow, Eq. 3.19 underestimates density near the free surface due to an "incompleteness" of W near the free-surface boundary, leading to the formation of an artificial particle boundary layer. The SPH continuity Eq. 3.18 produces more accurate estimates of density near the free surface as the (uniform initial) density evolves only in response to relative particle motion and, therefore, is less sensitive to the incompleteness of W. In addition, there is a computational advantage in using Eq. 3.18 because all rates of change can be calculated in one pass over the particles [54]. Whereas with Eq. 3.19, there is one pass to calculate the density then another to calculate the velocity gradient. Gomez-Gesteira et al. [55] used the velocity Verlet integration scheme with the continuity density computation approach. In their work, the SPH equations are integrated according to:

$$\mathbf{v}_i(t + \triangle t) = \mathbf{v}_i(t - \triangle t) + \frac{2\triangle t}{m_i}\mathbf{f}_i(t) \qquad (5.3)$$

$$\mathbf{r}_i(t + \triangle t) = \mathbf{r}_i(t) + \triangle t \mathbf{v}_i(t) + \frac{\triangle t^2}{2m_i}\mathbf{f}_i(t) \qquad (5.4)$$

$$n_i(t + \triangle t) = n_i(t - \triangle t) + 2\triangle t R_i(t), \qquad (5.5)$$

where $R_i(t) = \frac{dn_i(t)}{dt}(t)$. Once every N_s time steps ($N_s \approx 50$), variables are calculated according to a simpler forward Euler scheme (the Euler correction),

$$\mathbf{v}_i(t + \triangle t) = \mathbf{v}_i(t) + \frac{\triangle t}{m_i}\mathbf{f}_i(t)$$

$$\mathbf{r}_i(t + \triangle t) = \mathbf{r}_i(t) + \triangle t \mathbf{v}_i(t) + \frac{\triangle t^2}{2m_i}\mathbf{f}_i(t)$$

$$n_i(t + \triangle t) = n_i(t) + \triangle t R_i(t)$$

where $R_i(t) = \frac{dn_i(t)}{dt}$. Gomez-Gesteira et al. used the Euler correction to prevent divergence of the time integration scheme.

Liu et. at. [56] and Pan et al. [11] used the second-order leapfrog scheme to integrate continuity and momentum equations. In their approach, the position is computed at the integral timestep, whereas the density and velocity are computed at the half timestep. To keep the calculations consistent at the beginning of an iteration, density and velocity must be predicted at the integral timestep using

$$\mathbf{v}_i(t) = \mathbf{v}_i\left(t - \frac{1}{2}\triangle t\right) + \frac{\triangle t}{2m_i}\mathbf{f}_i(t - \triangle t)$$

$$n_i(t) = n_i\left(t - \frac{1}{2}\triangle t\right) + \frac{\triangle t}{2}R_i(t - \triangle t).$$

Then, this information is used to compute the standard leapfrog integration scheme as:

$$\mathbf{v}_i\left(t + \frac{1}{2}\triangle t\right) = \mathbf{v}_i\left(t - \frac{1}{2}\triangle t\right) + \frac{\triangle t}{m_i}\mathbf{f}_i(t)$$

$$n_i\left(t + \frac{1}{2}\triangle t\right) = n_i\left(t - \frac{1}{2}\triangle t\right) + \triangle t R_i(t)$$

$$\mathbf{r}_i(t + \triangle t) = \mathbf{r}_i(t) + \triangle t \mathbf{v}_i\left(t + \frac{\triangle t}{2}\right).$$

For all explicit SPH methods, the solution stability is governed by the following timestep constraints [37]:

$$\triangle t \leq 0.25 \min_i\left(\frac{h}{3|\mathbf{v}_i|}\right) \qquad (5.6)$$

$$\triangle t \leq 0.25 \min_i\left(\sqrt{\frac{m_i h}{3|\mathbf{f}_i|}}\right) \qquad (5.7)$$

$$\triangle t \leq \min_i\left(\frac{\rho_i h^2}{9\mu}\right), \qquad (5.8)$$

where $|\cdot|$ is the magnitude of a vector.

In the implicit ISPH formulation, the differential operators are implicitly non-linear functions of the particle positions, acting through the contribution of the gradient of the smoothing kernel $\nabla_\mathbf{r} W\left(|\mathbf{r} - \mathbf{r}_j|, h\right)$. To avoid a costly non-linear solution of the iterative method, in standard ISPH, the pressure is updated implicitly while fixing the particle positions to their value at the previous timestep. According to Eq. 4.7, the velocity also can be updated implicitly with the previous timestep's positions. The positions are usually updated explicitly using the midpoint quadrature.

$$\mathbf{r}_i(t + \triangle t) = \mathbf{r}_i(t) + \frac{\triangle t}{2}\left(\mathbf{v}_i(t) + \mathbf{v}_i(t + \triangle t)\right).$$

As mentioned previously, applying the implicit ISPH formulation removes the viscous timestep constraint in Eq. 5.8.

In some implementations of ISPH, the method is particularly sensitive to the so-called "tensile instability" in SPH. To prevent the associated clustering of particles, following the positions update, the particles are shifted, and an interpolation correction is applied. It should be noted that tensile instability can occur in both ISPH and WCSPH, and several alternative approaches exist for dealing with it in the ISPH [46] and WCSPH [57] methods. We also should note that adding pair-wise forces in the PF-SPH method plays a similar role as the repulsive forces in [57], and no tensile instability is usually observed in PF-SPH simulations.

5.1 Time integration errors

To study the accuracy of explicit time integration schemes, we consider SPH solutions of the coupled Euler and energy conservation equations:

$$\frac{d\mathbf{v}}{dt} = -\frac{\nabla p}{\rho} \tag{5.9}$$

and

$$\frac{\partial u}{\partial t} + (\mathbf{v} \cdot \nabla)u = -\frac{P}{\rho}\nabla \cdot \mathbf{v}, \tag{5.10}$$

where u is the internal energy per unit mass. Similar to Eqs. 3.14, 3.18, and 3.20, the SPH discretization of Eqs. 5.9 and 5.10 is given by:

$$m_i \frac{d\mathbf{v}_i}{dt} = \sum_j^N \mathbf{f}_{ij} \quad \mathbf{f}_{ij} = -\left(\frac{P_j}{n_j^2} + \frac{P_i}{n_i^2}\right)\frac{\mathbf{r}_{ij}}{r_{ij}}\frac{dW(r_{ij}, h)}{dr_{ij}} \tag{5.11}$$

and

$$\frac{du_i}{dt} = \frac{P_i}{\rho_i^2}\sum_{j=1}^N m_j(\mathbf{v}_i - \mathbf{v}_j) \cdot \nabla_i W(\mathbf{r}_{ij}, h). \tag{5.12}$$

We note that the right-hand side of Eq. 5.11 is antisymmetric with respect to indices i and j, i.e., $\mathbf{f}_{ij} = -\mathbf{f}_{ji}$. Therefore, the total momentum $\sum_i m_i \mathbf{v}_i$ is explicitly conserved. Conversely, the total energy $\sum_i m_i e_i$ (where $e_i = u_i + \frac{1}{2}\mathbf{v}_i \cdot \mathbf{v}_i$ is the energy of particle i per unit mass) is conserved only up to the SPH spatial discretization and time integration errors.

In the following, we study errors resulting from different explicit time integration schemes for a one-dimensional closed system. The model configuration is illustrated in Fig. 3. The SPH "fluid" particle is placed between the boundary particles on a straight line with the particle spacing $\Delta x = 0.05$ m. The fluid density is set to 1000 kg/m^3 (the density of water), which results in the particle mass $m_i = 50$ kg. In this study, we use the $P = c^2(\rho - \rho_0)$ EOS with the the speed of sound $c = 0.2$ m/s and the cubic kernel function W [37] with the smoothing length $h = 1.3\Delta x$.

Fig. 3 One-dimensional test configuration: *red* boundary particles and *blue* SPH fluid particle

Initially, the SPH fluid particle velocity is set to 0.01 m/s in the direction of the left boundary. Velocities of the boundary particles are set to zero to impose the no-flow boundary condition [55]. Then, the position, velocity, acceleration, and density are calculated according to the time integration schemes previously described. Figure 4 shows the variation of kinetic, internal, and total energy in the model for each time integration scheme.

From the energy variation plots shown, it is evident that in all time integration schemes, energy is correctly converted from kinetic to internal, and vice versa, as the fluid particle oscillates between the boundary particles. Though it appears that the total energy is conserved, inspection of the relative total energy error in Fig. 5 shows this is not the case.

Generally, the magnitude of total energy error for all considered integration schemes is less than 1 %. However, some differences are still observed, particularly between the Verlet and leapfrog methods, where the cause of the discrepancy is likely due to numerical imprecision. This occurs because the Verlet algorithm requires the addition of a second-order (in Δt) term to a relatively large first-order term in Eq. 5.1, which may produce roundoff effects [53].
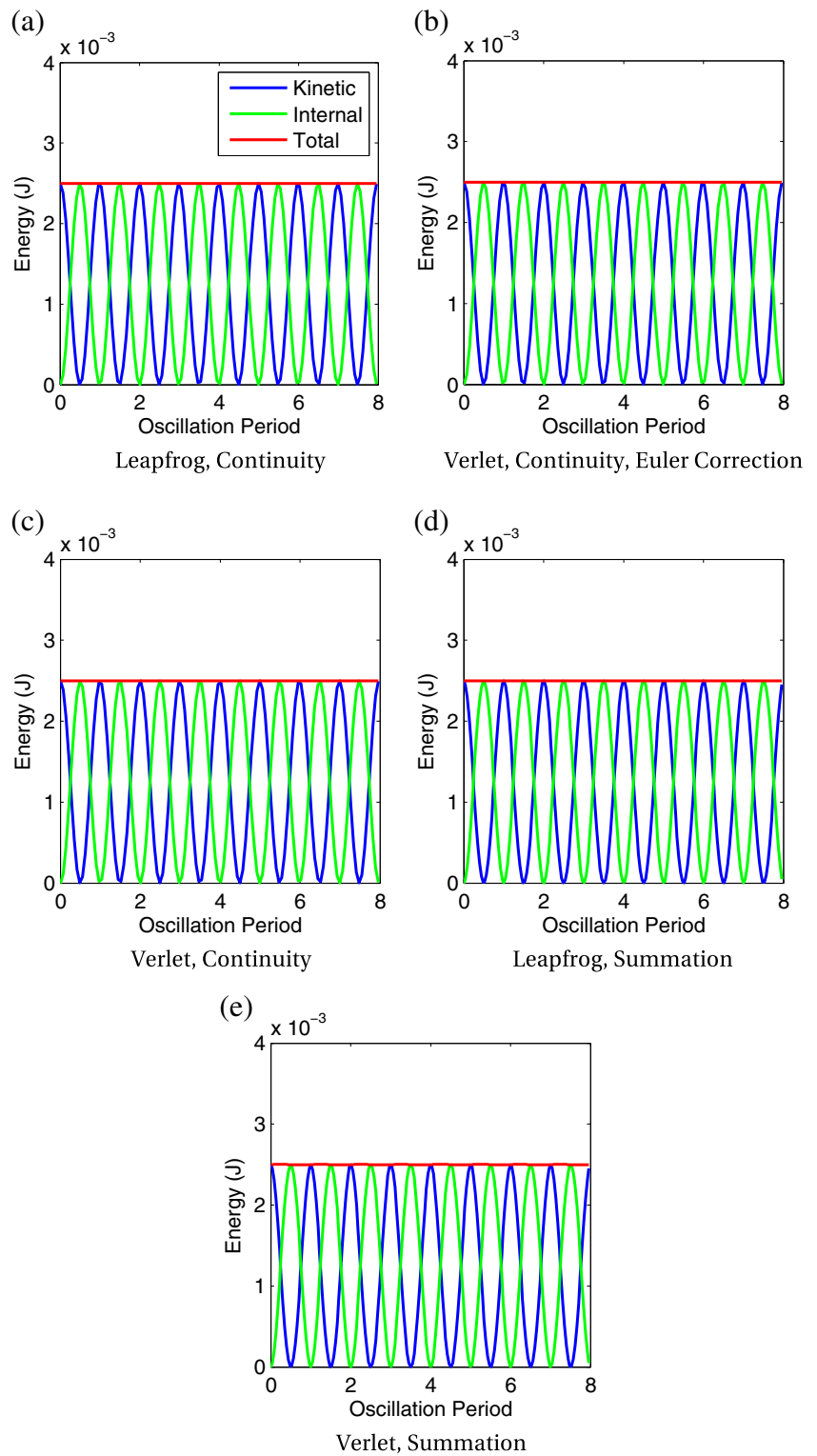
Another significant difference is obvious when comparing the relative total energy error of the Verlet methods using the continuity (Eqs. 5.3–5.5) and summation (Eqs. 5.1, 5.2, and 3.19) approaches. When the density summation approach is used, the average total energy error is extremely small, and the variation is consistent. However, when the Verlet scheme is applied with the continuity approach, the relative total energy error becomes very noisy, and grows in magnitude as the simulation proceeds. It should be noted that by removing the Euler correction, the average energy error becomes smaller. The errors associated with different integration schemes are summarized in Table 1.

Note that the total energy can be found directly from the equation $\frac{de}{dt} = -\frac{1}{\rho}\nabla \cdot (P\mathbf{v})$, which allows the conservative SPH discretization

$$m_i \frac{de_i}{dt} = -\sum_{j=1}^N \left(\frac{P_j \mathbf{v}_i}{n_j^2} + \frac{P_i \mathbf{v}_j}{n_i^2}\right) \cdot \nabla_i W(\mathbf{r}_{ij}, h). \tag{5.13}$$

The right-hand side of this equation is anti-symmetric with respect to indices i and j. Hence, the total energy $\sum_i m_i e_i$ of a closed system determined from this equation would be exactly conserved, regardless of the choice of time integration scheme. Therefore, in SPH simulations of non-isothermal flows, it is common to compute the total energy from Eq. 5.13 rather than Eq. 5.12.
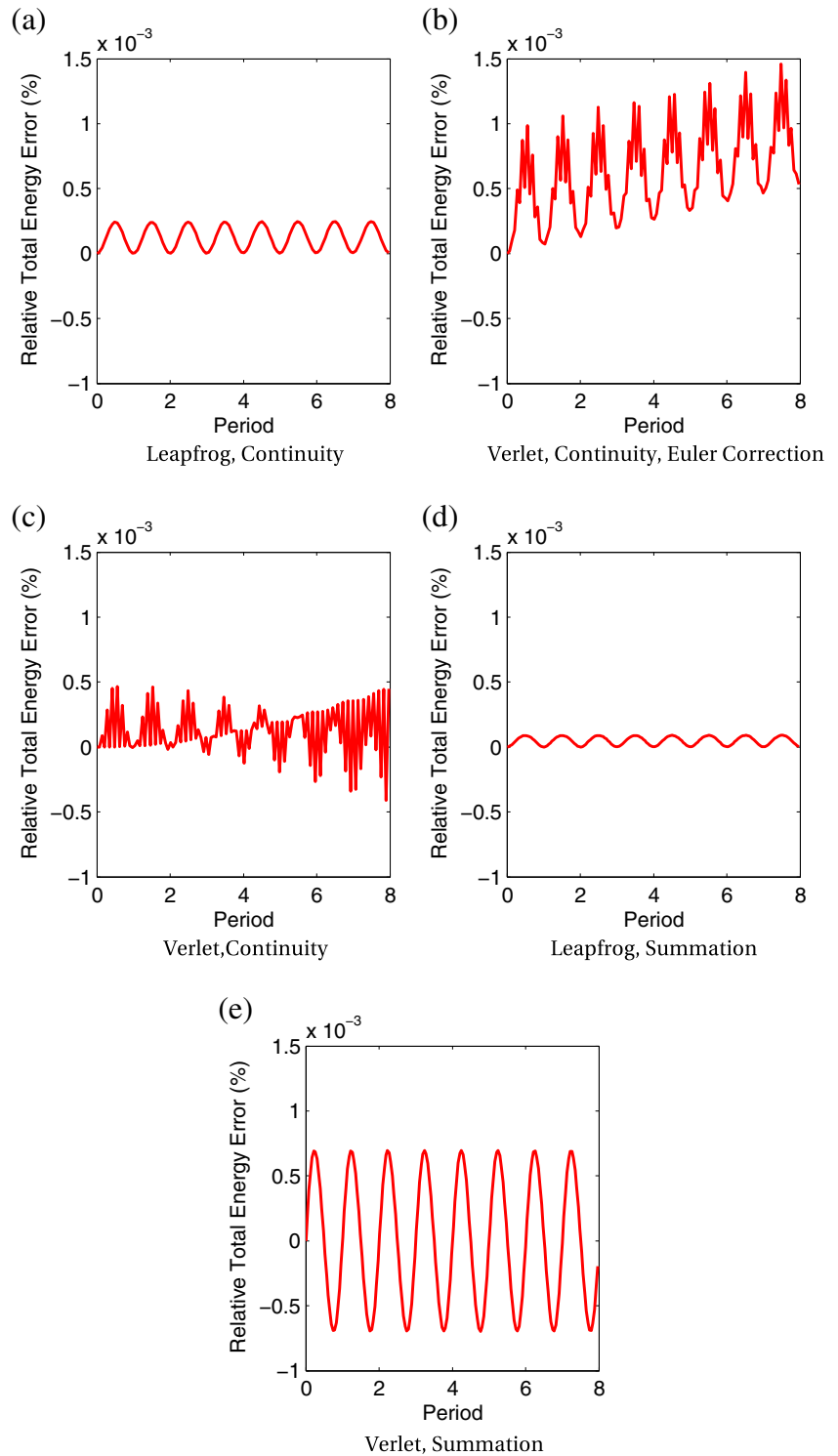
Fig. 4 Energy variation in 1D test case

(a)

Leapfrog, Continuity

(b)

Verlet, Continuity, Euler Correction

(c)

Verlet, Continuity

(d)

Leapfrog, Summation

(e)

Verlet, Summation

6 Boundary conditions for the Navier-Stokes equations

6.1 No-slip boundary condition

When the support of the kernel intersects the boundary of the domain for a given SPH particle, it is necessary to account for the truncated kernel support and enforce appropriate boundary conditions. While it is possible to do this by integrating by parts the SPH integral approximations of the spatial derivatives and directly evaluating the resulting boundary terms, this requires a discretization of the boundary and becomes computationally expensive for

Fig. 5 Relative Total Energy
Error in 1D Test Case

(a)

Leapfrog, Continuity

(b)

Verlet, Continuity, Euler Correction

(c)

Verlet,Continuity

(d)

Leapfrog, Summation

(e)

Verlet, Summation

geometrically complex domains. In the PF-SPH model, this problem is resolved by using "solid boundary" SPH particles that are included in summations in the momentum conservation Eq. 3.14. These particles "cover" the support of fluid SPH particles near the boundary. When the discrete operators are evaluated, values of velocity, density,

and viscosity are prescribed to the solid particles in such a way that appropriate boundary conditions are approximately enforced at the wall.

There are a number of approaches for determining "artificial" velocity values $\mathbf{v}_j^b$ at solid particle j. For the Dirichlet boundary condition $\mathbf{v}(\mathbf{x}, t) = \mathbf{v}_D(\mathbf{x}, t)$ on Γ_D, the simplest

Table 1 Mean and variance of relative total energy error

	Mean (%)	Variance (%)
Leapfrog, Continuity	1.28e-06	7.35e-13
Verlet, Continuity, Euler Correction	9.43e-06,	2.05e-11
Verlet, Continuity	1.19e-06	3.26e-11
Leapfrog, Summation	4.80e-07	9.86e-14
Verlet, Summation	2.78e-08	2.40e-07

approach is to set $\mathbf{v}_j^b = \mathbf{v}_D(\mathbf{x}^*, t)$, where $\mathbf{x}^*$ is the closest point on Γ_D to particle j. However, this approach introduces an $O(h)$ error and, when used to apply the no-slip boundary condition, results in a finite slip velocity at the wall. Review of the most common methods for implementing the Dirichlet boundary conditions for the NS equations and the corresponding error analysis can be found in [58].

The most common extrapolation method for applying Dirichlet boundary conditions for the NS equations was proposed originally by Takeda et al. [59]. Later, this method was used by Morris [37] to model flow in porous media. In the Takeda-Morris approach, when calculating the difference in velocities of fluid and boundary particles $\mathbf{v}_i - \mathbf{v}_{j|i}^b$ in the force (3.15), the artificial velocity of the solid particle j with respect to fluid particle i is found by linear extrapolation

$$\mathbf{v}_{j|i}^b = -\frac{d_j^b}{d_i} \mathbf{v}_i, \tag{6.1}$$

where the distances d_j^b and d_i are the closest perpendicular distances to the wall of boundary particle j and fluid particle i, respectively. For the homogeneous Neumann boundary condition, $\mathbf{v}_i - \mathbf{v}_j^b = 0$ is enforced instead.

For straight wall or circular boundaries, calculations of d_j^b and d_i can be performed relatively easily. For more complex boundaries, these calculations become non-trivial, and for boundaries with sharp corners, d_j^b and d_i may not be uniquely defined. To address this, Holmes et al. [43] proposed to approximately compute the distance from a particle to the interface as follows:

$$d_i = \frac{h}{0.5} (\kappa_i - 0.5), \tag{6.2}$$

where

$$\kappa_i = \frac{\sum_{j=1}^{N} \delta_{ij} W\left(|\mathbf{r}_i - \mathbf{r}_j|, h\right)}{\sum_{j=1}^{N} W\left(|\mathbf{r}_i - \mathbf{r}_j|, h\right)} \tag{6.3}$$

and δ_{ij} is equal to 1 if particles i and j are both either fluid or boundary particles and zero otherwise. Figure 6 demonstrates the smoothed approximation of Eq. 6.2 of the
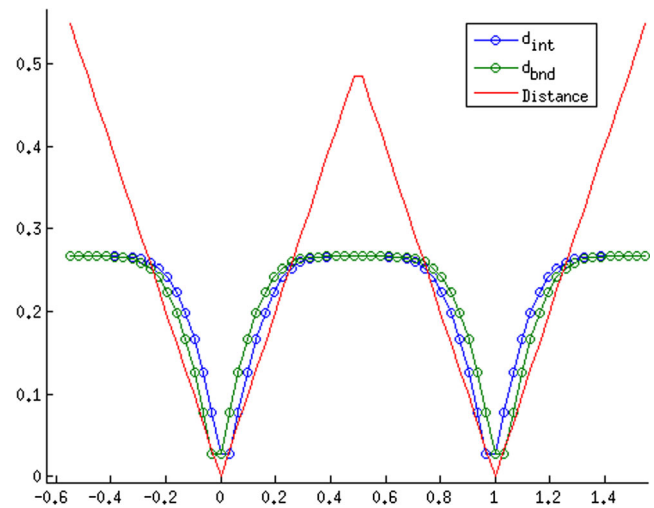
Fig. 6 Smoothed approximation of the distances to the wall d_i and d_b for a simple 1D channel flow geometry. In this example, the distance to the wall at $x = 0$ and $x = 1$ is approximated using Eq. 6.2. (After [43])

distance function for a one-dimensional channel flow. It should be noted that Eq. 6.2 can be only used to calculate distances for particles within distance h from the boundary.

Figure 7 shows the transient velocity profile for two-dimensional flow between two parallel plates. The solid line denotes the analytical solution, and asterisks show the solutions obtained from the SPH simulations, where the boundary particles velocities were set to zero. Circles represent the solution obtained from the SPH simulations with the artificial velocities of boundary particles computed from Eq. 6.1. It is evident that the Takeda-Morris approach produces a more accurate velocity profile but at the additional cost of computing normal distances to the boundary. Another approach, the continuum boundary force (CBF) method, was recently proposed in [60] for solving the NS equations subject to the Robin boundary condition describing a partial velocity slip at the boundary. It was demonstrated that the CBF method can be also used to model the no-slip boundary conditions at a limiting case of the Robin boundary condition. The CBF method is an extension of the continuum surface reaction(CSR) method [61–63] for advection-diffusion equations subject to the Robin (reactive) boundary condition. The CBF and CSR methods are described in Sections 6.2 and 10, respectively.

6.2 Partial slip boundary condition

Under most natural conditions, it is reasonable to assume that the velocity field in the pore-scale models satisfies the no-flow boundary condition (2.6). This is because, for simple wetting fluids, the slip length (the outer normal distance from the boundary to where the fluid velocity is
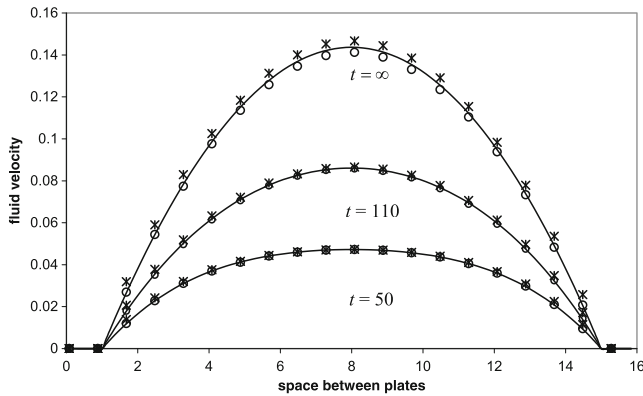
Fig. 7 Transient velocity profiles for flow between two parallel plates subject to the no-flow boundary condition. The *solid lines* are velocity profiles obtained analytically, and *asterisks and circles* represent velocity profiles obtained from SPH simulations with two different approaches to modeling the solid boundary. The *asterisks* show the results of a PF-SPH simulation obtained with zero velocities of the boundary particles. The *circles* indicate the results obtained using the approach proposed in [37] for treating no-slip boundary conditions at solid surfaces. In the simulations, the flow is driven by a constant body force, and the SPH momentum conservation equation is discretized according to Eqs. 3.14 and 3.20. (After [52])

extrapolated to become zero) is on the order of molecular size and in pore-scale simulations can be set to zero. On the other hand, for non-wetting fluids (such as oil), the slip length can be in the range of 10–15 nm [64], and for flow in nano- and micron-size pores, the slip length cannot be set to zero without introducing significant errors. In some complex flows (e.g., flow of supercritical carbon dioxide in the presence of the residual water film) and near a fluid-fluid-solid contact line, the slip length can be significantly larger.

In general, velocity slip at the boundary is described by the Robin boundary condition

$$\boldsymbol{\tau}(\mathbf{x}_s, t) \cdot \mathbf{n}(\mathbf{x}_s) = \mathbf{f}_\Gamma(\mathbf{x}_s, \mathbf{v}) \quad \mathbf{x}_s \in \Gamma, \tag{6.4}$$

or its linear form, the Navier boundary condition, corresponding to $\mathbf{f}_\Gamma(\mathbf{x}_s, \mathbf{v}) = \beta \mathbf{v}$, where β is a constant inversely proportional to the slip length. Two limiting cases of the Navier slip boundary condition include (1) $\beta = 0$, corresponding to the free-slip boundary condition, and (2) and $\beta = \infty$, corresponding to the no-slip condition (i.e., $\mathbf{v} = 0$).

A direct implementation of the Robin boundary condition in SPH can be difficult, especially if the boundary is geometrically complex. Similar difficulties exist in the grid-based finite difference and finite volume methods, which have led to the development of approximate methods that replace the boundary condition with a continuous forcing field such as the immersed boundary method [65] and the diffuse domain method [66]. In the context of SPH, a so-called continuum boundary force (CBF) method was

recently proposed [60]. In the CBF method, the boundary Γ is replaced with a diffused region of the thickness $2h$ centered on Γ. Then, the NS equations subject to the Robin BC are approximated with the momentum conservation equation

$$\begin{aligned}
\rho^r(\mathbf{x}, t) \frac{d\mathbf{v}^r(\mathbf{x}, t)}{dt} &= -\nabla P^r(\mathbf{x}, t) + \nabla \cdot \boldsymbol{\tau}^r(\mathbf{x}, t) + \rho^r(\mathbf{x}, t)\mathbf{g} \\
&\quad -\mathbf{f}_\Gamma(\mathbf{x}, \mathbf{v}^r) \iiint_{\Omega_S} [\mathbf{n}(\mathbf{x}) + \mathbf{n}(\mathbf{x}')] \\
&\quad \cdot \nabla_\mathbf{x} W(\mathbf{x} - \mathbf{x}', h) d\mathbf{x}', \\
&\quad \mathbf{x} \in \Omega_F,
\end{aligned} \tag{6.5}$$

subject to the homogeneous Neumann boundary condition

$$\boldsymbol{\tau}^r(\mathbf{x}_s, t) \cdot \mathbf{n}(\mathbf{x}_s) = 0, \quad \mathbf{x}_s \in \Gamma. \tag{6.6}$$

Here, the computational domain is extended to $\Omega = \Omega_F \cup \Omega_S$, where Ω_S is the extension of Ω_F, i.e., $\Omega_F \cap \Omega_S = 0$. The kernel W is the standard SPH kernel, and its support h determines the size of the diffused boundary region. In the limit $h \to 0$, the CBF formulation recovers the standard NS equations, i.e.,

$$\lim_{h \to 0} \mathbf{v}^r = \mathbf{v}, \quad \lim_{h \to 0} \rho^r = \rho, \quad \lim_{h \to 0} P^r = P. \tag{6.7}$$

As in PF-SPH model, the domains Ω_F and Ω_S are discretized with "fluid" and "solid" particles, respectively. A weakly compressible SPH discretization of Eq. 6.5 subject to the boundary condition (6.6) can be written as [60]:

$$\begin{aligned}
m_i \frac{d\mathbf{v}_i}{dt} &= -\sum_{j \in \Omega} \left(\frac{P_j}{n_j^2} + \frac{P_i}{n_i^2} \right) \frac{\mathbf{r}_{ij}}{r_{ij}} \frac{dW(r_{ij}, h)}{dr_{ij}} \\
&\quad + \sum_{j \in \Omega_P} \frac{4\mu_i \mu_j}{\mu_i + \mu_j} \frac{\mathbf{v}_{ij}}{n_i n_j r_{ij}} \frac{dW(r_{ij}, h)}{dr_{ij}} \\
&\quad + m_i \mathbf{g} - \sum_{k \in \Omega_S} \mathbf{F}_{ik}^b,
\end{aligned} \tag{6.8}$$

where $\sum_{j \in \Omega}$ denotes summation over all fluid and solid particles, $\sum_{j \in \Omega_F}$ assumes summation over fluid particles only, and $\sum_{j \in \Omega_S}$ denotes summation over solid particles only. In [60], the "artificial viscous stress" approximation of the divergence of the viscous stress was used [9], which is applicable for modeling both incompressible and compressible flows. The homogeneous Neumann boundary condition (6.6) is enforced by performing summation over only fluid particles when computing viscous force in Eq. 6.8, as commonly done in SPH free-surface flow models [38]. The

boundary force term $\mathbf{F}_{ik}^b$ is obtained by discretizing the integral in the CBF Eq. 6.5 as follows:

$$\mathbf{F}_{ik}^b = \beta(\mathbf{x} = \mathbf{r}_i, \mathbf{v}_{ik})\mathbf{v}_{ik}\frac{1}{n_i n_k}(\mathbf{n}_i + \mathbf{n}_k) \cdot \nabla_i W(\mathbf{r}_{ik}, h), \quad (6.9)$$

and the normal unit vector $\mathbf{n}_i$ is found as:

$$\mathbf{n}_i = \frac{\sum_{j \in \Omega}\frac{1}{n_j}(\psi_j - \psi_i)\nabla_i W(\mathbf{r}_{ij}, h)}{\left|\sum_{j \in \Omega}\frac{1}{n_j}(\psi_j - \psi_i)\nabla_i W(\mathbf{r}_{ij}, h)\right|}, \quad (6.10)$$

where ψ is the color function defined as:

$$\psi(\mathbf{x}) = \begin{cases} 1, & \mathbf{x} \in \Omega_S \\ 0, & \mathbf{x} \in \Omega_F. \end{cases} \quad (6.11)$$

Figure 8 shows a two-dimensional velocity field obtained from an CBF-SPH simulation of flow around a "sunflower"-shaped obstacle subject to the Navier boundary condition. This figure also shows a good agreement between the velocity profiles obtained from the CBF-SPH and finite element methods for several slip lengths (including a large β ($\beta = 10$), corresponding to the no-slip condition) and $\beta = 0$.

In [60], the CBF method was also tested for a three-dimensional flow of water between two planes located at $y = 0$ and $H = 0.1$ m. The bottom plane was assumed to be chemically heterogeneous and characterized by a spatially varying slip length. The free-slip boundary condition was imposed at the upper plane. The NS equations were

solved subject to the initial condition $v_x = 10^{-5}$ m and $v_y = v_z = 0$, the Robin boundary conditions at the top and bottom planes,

$$\begin{cases} \boldsymbol{\tau} \cdot \mathbf{n} = \beta[1 + \sin(\omega x)\sin(\omega z)]\mathbf{v} & \text{at } y = 0 \quad 0 \le x, z \le H \quad t > 0, \\ \boldsymbol{\tau} \cdot \mathbf{n} = 0 & \text{at } y = H \quad 0 \le x, z \le H \quad t > 0, \end{cases}$$
$$(6.12)$$

and the periodic boundary condition at the rest of the boundaries. Figure 9 depicts the comparison of velocity profiles at time $t = 55.3$ s, determined from the SPH-CBF and finite element methods. A good agreement is observed between the two methods.

7 Single phase flow simulations

The simplest application of SPH for flow in porous media involves modeling a single-phase flow at the pore scale (e.g., [37, 43, 67]). Single-phase SPH pore-scale flow models have been used to compute transport properties of the porous media (permeability, tortuosity, dispersivity) and the Lagrangian statistics of fluid velocity and particle displacements. The latter is difficult to determine from grid-based Eulerian methods. For example, in [5], the Lagrangian velocity statistics, determined from an SPH simulation, have been used to parameterize the correlated continuous time random walk (CCTRW) model. In [6], the SPH model
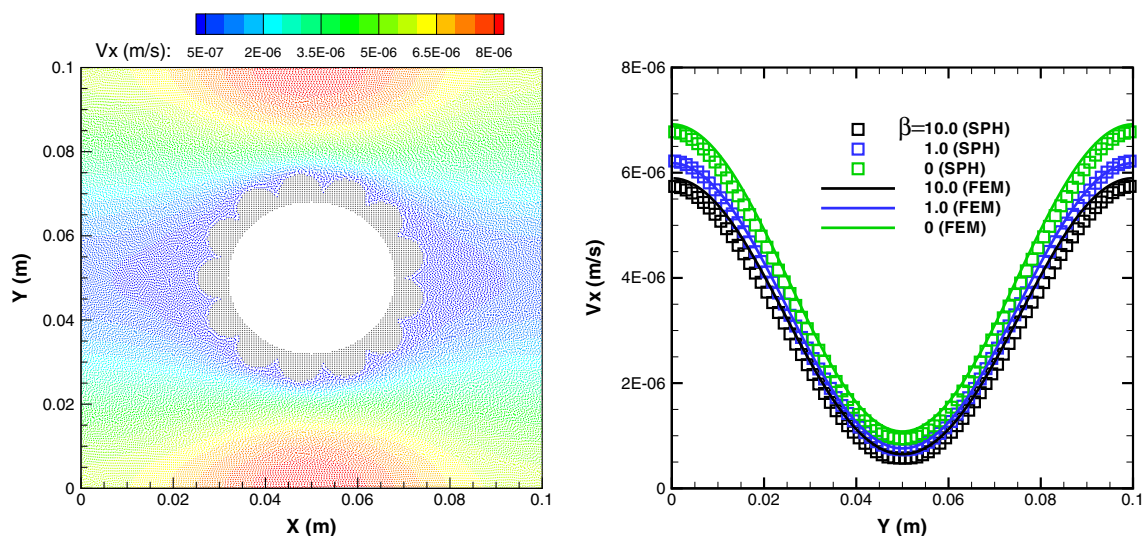
Fig. 8 Two-dimensional flow around the "sun-flower"-shaped obstacle subject to the Navier boundary condition with $\mathbf{f}_\Gamma = \beta\mathbf{v}$ at the fluid-solid boundary and the periodic boundary conditions at the external boundaries. The flow is driven by the body force acting in the x direction. *Left* A snapshot of the distribution of SPH particles obtained from the simulation with $\beta = 10$ after the flow had reached its steady state. Gray particles represent solid particles. The color scale denotes magnitude of the x component of the velocity of the fluid particles. *Right* Comparison of $\mathbf{v}_x$ profiles along the line at $x = 0.1m$ for $\beta = 0.0, 1.0, 10.0$ with the spatial resolution $\Delta x = 5.0 \times 10^{-4}$m and $Re = 0.1 - 0.2$, obtained with the CBF-SPH and finite element methods (After [60])

Fig. 9 The contour plots (projection on x-z plane (*left*) and slices in y-z plane (*right*)) of the velocity component $\mathbf{v}_x$ obtained with the CBF-SPH and finite element methods. In these simulations, $\beta = 0.1$ in Eq. 6.12 and the Reynolds number is $Re = 1$ (After [60])
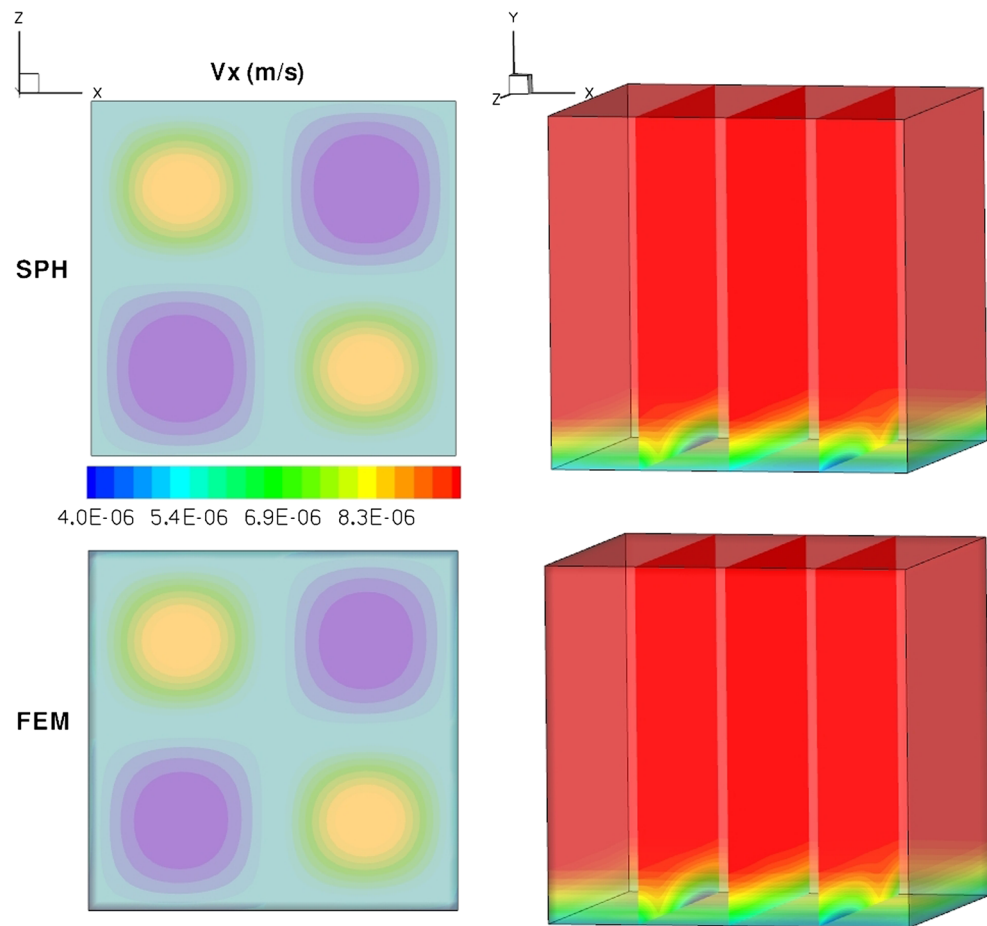
was used to compute statistics of particle displacements and the coefficient of mechanical dispersion in an effective stochastic reactive transport model.

Holmes et al. [43] and Pereira et al. [67] used SPH to model flow in three-dimensional porous media and demonstrated convergence of the SPH solutions for the effective parameters, including permeability and friction coefficient. Holmes et al. also showed that to obtain a reasonably accurate solution, the pore throats should be "discretized" with, at least, 30 SPH particles.

Ovaysi and Piri [7] used an incompressible version of a modified SPH method, known as the moving particle semi-implicit (MPS) method to model single-phase pore-scale flow in a 1.02 x 1.02 x 1.02 mm^3 sandstone sample with 3.398 μm resolution. The pore geometry was reconstructed from three-dimensional high-resolution micro-computed-tomography (micro-CT) images of rock samples. To model a domain of this size, adaptive splitting and coalescence of SPH particles (analogous of adaptive resolution in grid based methods) was used in [7]. The simulations were used to compute the permeability of the sandstone, and the

computed values were found to be in a close agreement with the permeability values obtained from the experiments.

8 Two-phase flow simulations

To date, most of SPH pore-scale studies of multiphase flow have used the weakly compressible PF-SPH formulation. Validation of the PF-SPH model for multiphase and free-surface problems under static and dynamic conditions allowing analytical solutions has been done in [17, 51, 52]. In [25], the PF-SPH method was used to model displacement of one fluid by another in a microcell for a wide range of Capillary numbers, Ca, and viscosity ratios, M, and the results of the simulations were compared with the laboratory experiments of [68]. Figure 10 presents the $M - Ca$ phase diagram developed in [68] based on the laboratory displacement experiments. Solid lines in Fig. 10 show boundaries of the regions in the $M - Ca$ space where the displacement takes the form of viscous fingering, capillary fingering, and stable displacement. Symbols in Fig. 10
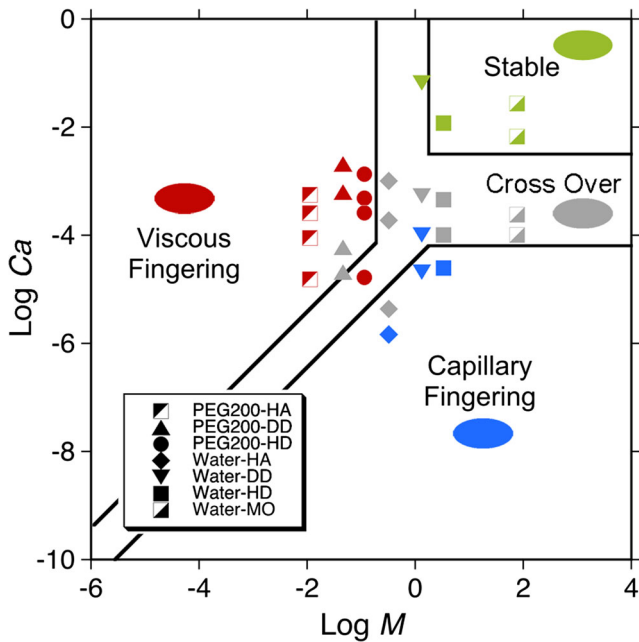
Fig. 10 Different types of displacements, obtained from SPH simulations of a wetting fluid being displaced by a non-wetting fluid), plotted on the phase diagram developed by [68]. *Continuous lines* represent the boundaries of viscous fingering, capillary fingering, and stable displacement regions. The legend lists fluids used in each experiment. The terms PEG200, HA, DD, HD, and MO correspond to polyethylene glycol 200, hexane, dodecane, hexadecane, and mineral oil, respectively. The porous domain is initially filled with a wetting fluid (water or PEG200) (After [25])

denote the combinations of Ca and M for which the corresponding SPH simulations were conducted. The color of the symbols corresponds to the three different types of displacement observed in the simulations. This figure shows a good agreement between displacement types obtained in the SPH simulations and observed in the experiments.

Figure 11 provides a side-by-side comparison of the experiments in [68] and the corresponding PF-SPH simulations for three combinations of M and Ca, corresponding to the viscous fingering, capillary fingering, and stable displacement regimes. Figure 12 compares steady-state non-wetting fluid saturations (S_{nw}) for different Ca and M obtained from the simulations and experiments. A good qualitative and quantitative agreement, observed in these figures, shows that the PF-SPH model is able to simulate various types of displacements for the wide range of flow conditions and fluid properties.

One of the advantages of SPH model is that it can simulate multiphase fluid flow with large density and viscosity ratios. In [1, 69], the PF-SPH model was used to simulate flow of water and air (unsaturated flow) in porous media. In these simulations, the density and viscosity ratios of liquid to gas phases were set to 1000 and 100, respectively. In

[1], the PF-SPH model was used to study the effect of pore-scale heterogeneity on the pressure-saturation relationship. In the simulations, the water was drained by incrementally increasing capillary pressure, defined as $P_c = \delta\rho g H$, where $\delta\rho$ is the difference in the density of the liquid and gas phases, g is the magnitude of the body force per unit mass, and H is one half the size of the simulation domain in the vertical direction (the direction of the body force action). In the simulations, P_c was changed by increasing g. Two two-dimensional artificial porous media were considered. One was made of non-overlapping circular grains with a micro-fracture running through the middle of the domain. The second porous medium was made of non-overlapping co-oriented elliptical soil grains. Figure 13 compares the distributions of liquid and gas phases obtained as a result of liquid phase drainage for the fracture, oriented parallel and perpendicular to the direction of the body force. Figure 14 compares distributions of the liquid and gas phases obtained as a result of drainage for the soil grains, oriented parallel and perpendicular to the direction of the body force. Both figures show that anisotropy has significant effect on the distribution of the fluid phases. Figure 15 compares saturation as a function of Bond number (the dimensionless capillary pressure defined as $Bo = P_c l^2 / (\sigma H)$, where l is the soil grain diameter). The main conclusion of this work is that, in the presence of pore-scale anisotropy, the $P_c - S$ relationship may depend on the flow direction. In the same work, the PF-SPH model was also used to study the effect of the static contact angle on two-phase flow.

In [69], the advantage of the SPH Lagrangian framework for interface tracking was exploited to study interactions between "old" and "new" water in porous media. The PF-SPH model was used to model consequent infiltration-drainage cycles. Figure 16 shows distributions of the old water and new water and the air phase obtained from the SPH simulations. This study found that pockets of old water may remain almost intact for a long time during infiltration of new water. It was suggested that such interplay between old and new water may play a significant role in the chemical signature of water in the unsaturated zone and aquifer.

9 Free surface flow

Free surface problems describe dynamics of liquid and gas phases where the gas phase is continuous. As a result of the very high ratio of the liquid and to gas viscosities, the dynamics of the continuous gas phase does not have significant impact on the liquid flow, and the pressure of the gas phase can be assumed uniform. Therefore, free-surface problems are formulated as the NS equations defined on

Fig. 11 a Viscous finger
formed by hexane displacing
polyethylene glycol, log
M = −1.95 and log Ca = −4.57.
b Capillary fingers formed by
hexane displacing water, log
M = −0.49 and log Ca = −3.38.
c Capillary fingers formed by
mineral oil displacing water, log
M = 1.88 and log Ca = −1.30. In
all simulations, the non-wetting
fluid is injected through the
left-hand side boundary with a
constant rate. The constant flux
boundary condition is prescribed
at the outlet (the right-hand side
vertical boundary) (After [25])

(a)

(b)

(c)
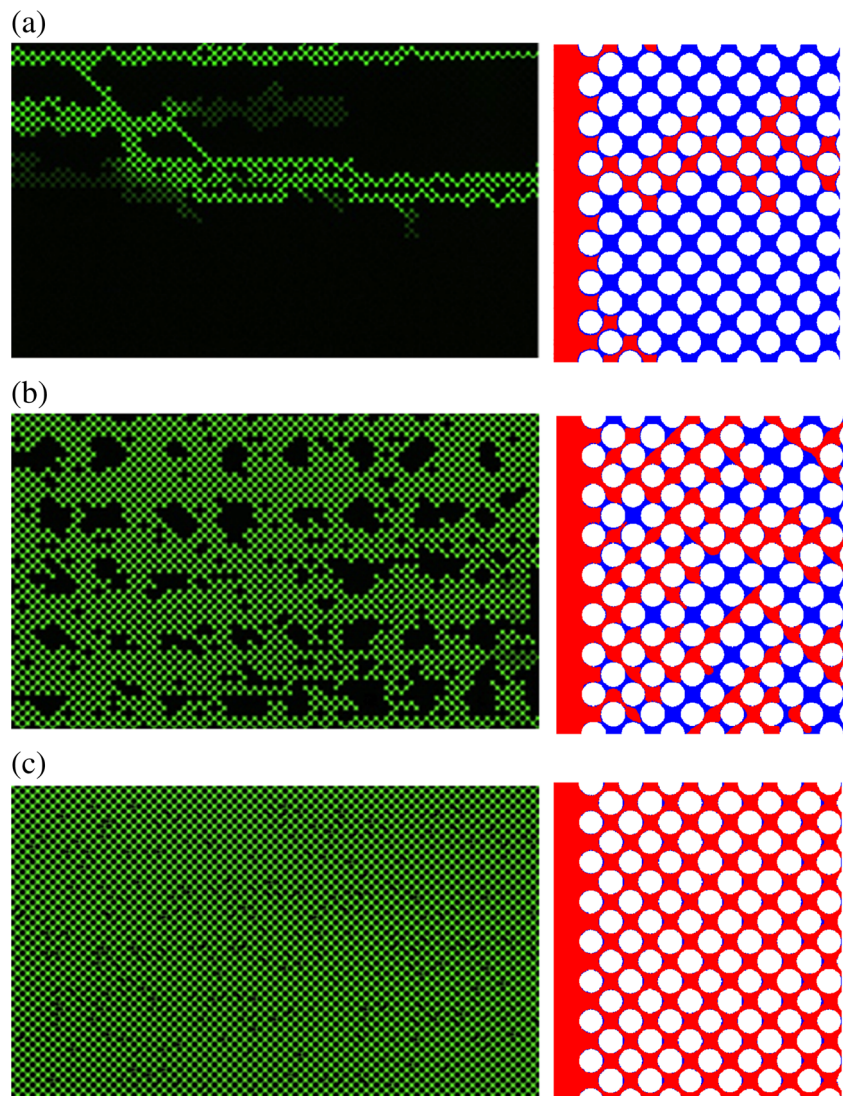
the domain occupied by the liquid phase and subject to the free-surface boundary condition on the liquid-gas interface

$$Pn = -\tau_w \cdot n + \kappa\sigma n \quad x \in \gamma. \tag{9.1}$$

In numerical models based on the phase field, level set, and similar indirect front tracking methods, both the liquid and gas phases must be modeled as the phase field, or the level set function has to be advected on both sides of the interface. Because of this, these methods are not very efficient for free-surface problems.

One advantage of the PF-SPH method for free surface problems is that it does not require discretizing the gas phase (and solving equations for the gas phase). In [51, 52], the PF-SPH method was used to solve the NS equations subject to the free-surface boundary condition. In these studies,

Eq. 3.19 was used to calculate particle density, and the van der Waals EOS

$$P = \frac{k_b T n}{1 - bn} - an^2 \tag{9.2}$$

was used to compute pressure. Here, k_b is the Boltzmann constant, n is the number density, T is the temperature, and a and b are the van der Waals constants. Comparisons with analytical solutions for relatively simple flows, laboratory experiments for the droplet flow through an inverted "Y"-shaped fracture junction, and the droplet flow at critical state on inclined flat surfaces demonstrated that this approach can accurately model surface-tension-dominated free surface flows [20, 51, 52].

In [20], the PF-SPH free surface model was used to study the effect of the residual fluid film on the velocity of a droplet sliding down the surface under gravity. It was

Fig. 12 Saturation of non-wetting phase versus Ca for different M. Comparison of SPH results with micromodel experiments of Zhang et al. [68] (After [25])

(a)

log M=-0.49

(b)

log M=0.12

(c)

log M=0.52

(d)

log M=1.88
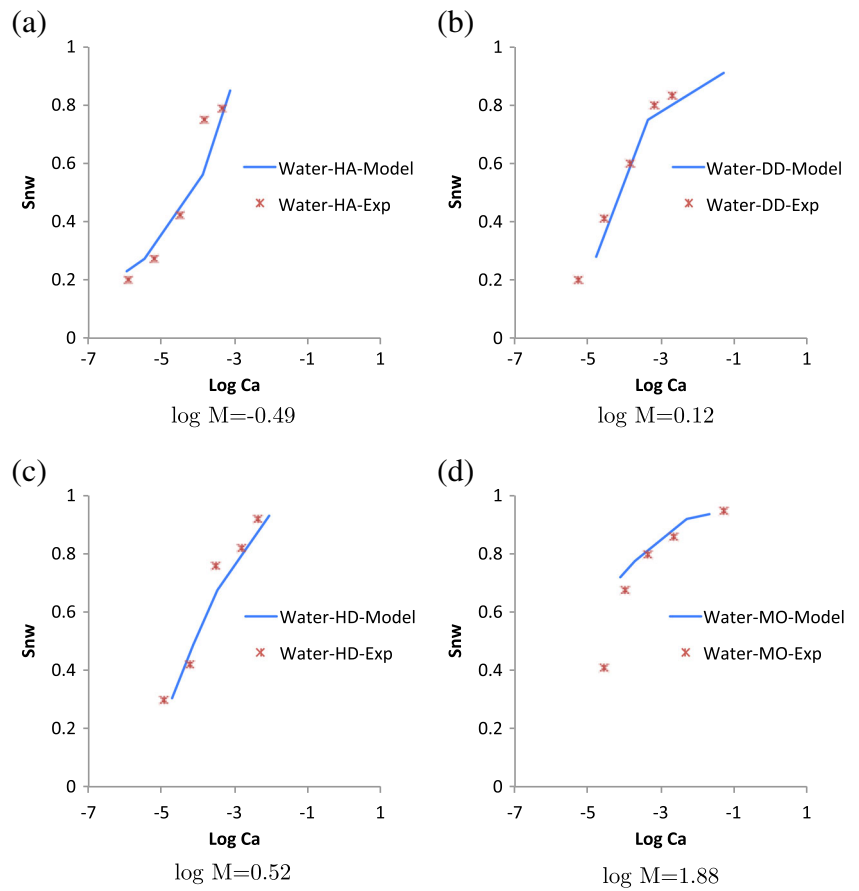
Fig. 13 Equilibrium distribution of a strongly wetting liquid for three different Bond numbers during drainage of the liquid from a porous medium containing a microfracture: **a** vertically oriented fracture and **b** horizontally oriented fracture. Liquids are drained in the vertical direction by an incremental increase in the Bond number. Black particles denote soil grains and impermeable boundaries of the flow domain, light gray particles represent gas phase, and dark gray particles represent liquid phase (After [1]).

(a)

$S = 0.72$ $S = 0.47$ $S = 0.35$

(b)

$S = 0.6$ $S = 0.37$ $S = 0.3$

Bo = 1.41   Bo = 2.83   Bo = 5.66
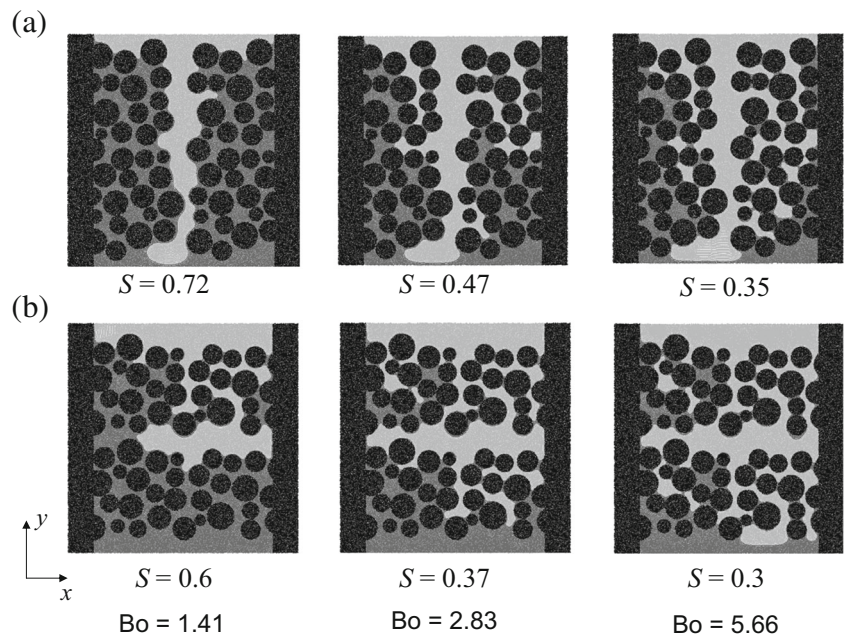
Fig. 14 Equilibrium distribution of a strongly wetting liquid during liquid drainage from anisotropic porous media for three different Bond numbers: **a** major axes of soil grains are aligned in the vertical direction and **b** major axes of soil grains are aligned in the horizontal direction. Liquids are drained in the vertical direction by an incremental increase in the Bond number. Black particles denote soil grains and impermeable boundaries of the flow domain, light gray particles represent the gas phase, and dark gray particles represent the liquid phase (After [1])
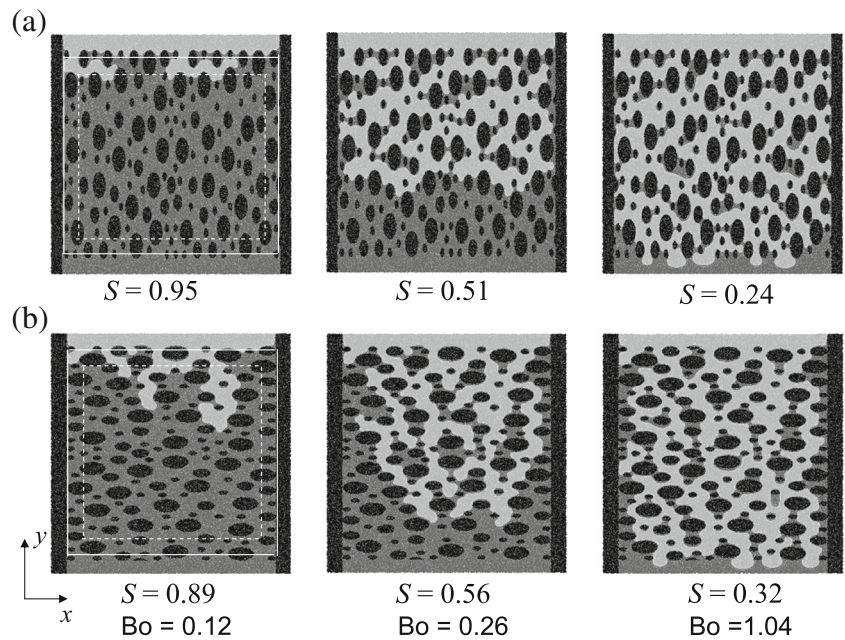
found that droplets move faster on wet surfaces than on dry surfaces. The effect of the residual film increases with increasing viscosity of the liquid. In [20], droplet flow on rough surfaces was also considered, (see Fig. 17). Surfaces with a self-affine fractal geometry with Hurst exponents ζ = 0.75, 0.50, and 0.25 (the roughness of the surface decreases with increasing ζ) were generated according to [52]. In the simulations, the surface inclination was set to 90 and 45°, and the static contact angle was set to $\theta_0 = 110$, 80, and 60°. Figure 18 shows the resulting dimensionless velocity of a droplet $Re = \frac{\rho v V^{1/3}}{\mu}$ (V is the volume of the droplet) as a function of ζ ($\zeta = 1$ corresponds to a smooth surface). It was found that surface roughness reduces the velocity of droplets. For example, droplets with $\theta_0 = 110$ and

80° experienced a velocity decrease between 33 and 37 % on the surface with $\zeta = 0.75$ compared to the smooth surface, regardless of the surface inclination. For a droplet with $\theta_0 = 60$°, the velocity decreased by as much as 80 % for an inclination angle of 90° and 98 % for an inclination angle of 45°. For lower ζ, i.e., "rougher" surfaces, a droplet with $\theta_0 = 60$° barely moved, while for higher contact angles, the velocity decreased proportionally to ζ.

Evaluation of the density near the free surface can be significantly improved using the SPH discretization of the continuity Eq. 3.18 instead of Eq. 3.19 [11, 38]. Our tests show that this would also eliminate the need for using the van der Waals EOS, and the more traditional EOS, such as Eqs. 4.2 and 4.3, could be used. Another attractive
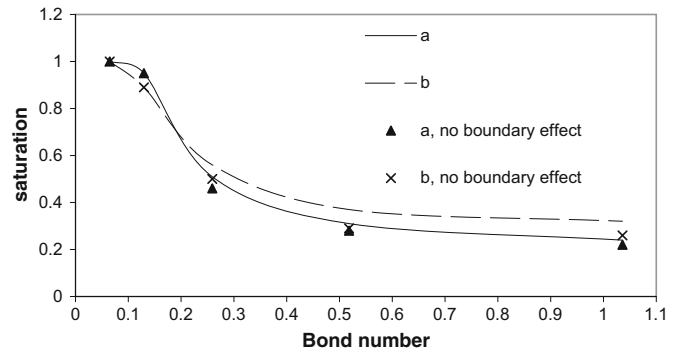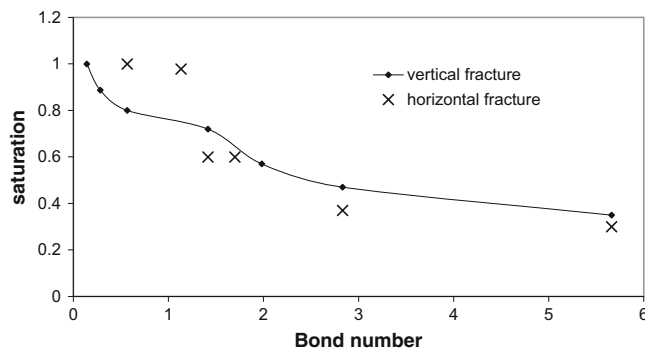
Fig. 15 **a** Saturation versus Bond number as a function of the fracture orientation. Drainage of a strongly wetting liquid in response to the incremental increase in the Bond number. **b** Effect of orientation of the anisotropic porous medium on the S/Bo relationship for the strongly wetting liquid drained by incremental increases in the Bond number. (1) *Solid line*: vertical particle alignment; S/Bo relationship

is estimated for the whole domain. (2) *dashed line*: horizontal particle alignment; Pc/S relationship is estimated for the whole domain. (3) *triangle symbols*: vertical particle alignment; S/Bo relationship is estimated for the domain bounded by the *dashed line* in Fig. 14. (4) *X symbols*: horizontal particle alignment; S/Bo relationship is estimated for the domain bounded by the *dashed line* in Fig. 14 (After [1])
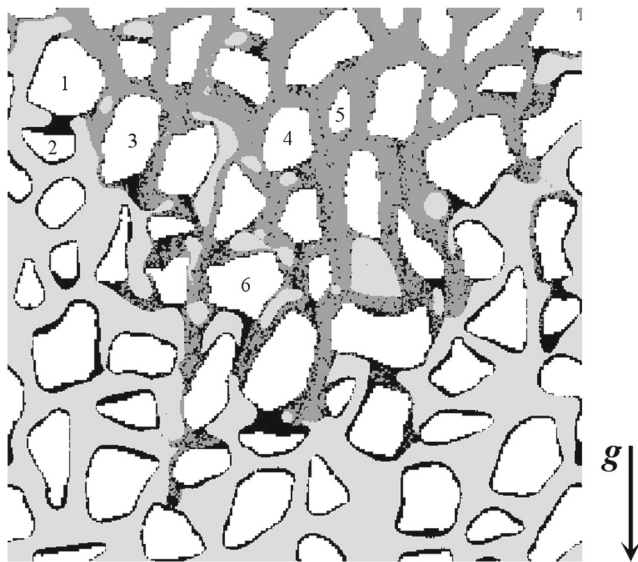
Fig. 16 Infiltration of "new water" in a pore space wetted by "old water." *Black* denotes the old water, *dark gray* depicts the new water, *light gray* represents the air, and *white* represents the quartz grains. Flow is driven by gravity only. The effect of surface tension is clearly visible between grains 1 and 2. Below grain 3, a pocket of old water is dragged by the new water but does not mix with it. Old water is mixed with new water between grains 4 and 5. Air bubbles are trapped around grain 6 (After [69])

alternative is to use the projection approach to solve PF-SPH equations subject to a divergence-free velocity condition to eliminate the need for an equation of state.

It should be noted that for the weakly compressible free-surface PF-SPH model, Eqs. 3.37 and 3.38, do not provide an accurate relationship between the surface tension and parameters in the pair-wise forces. Therefore, the weakly compressible free-surface PF-SPH model must be calibrated for a given surface tension and static contact angle. This can be due to particle density variations near the free surface (that are absent in the multiphase PF-SPH model) that violate the assumption of constant density used to derive Eqs. 3.37 and 3.38. It would be interesting to see if the incompressible PF-SPH method would produce the surface tension and static contact angle satisfying Eqs. 3.37 and 3.38.

10 Reactive transport, microbial growth, and mineral precipitation

Reactive transport of M chemical species can be described by the advection-diffusion-reaction equation defined on the domain Ω_P,

$$\frac{DC^m}{Dt} = \frac{1}{\rho}\nabla \cdot \left(\rho D^m \nabla C^m\right) + \frac{1}{\rho}r^m\left(C^1, ..., C^M\right),$$
$$m = 1, M \quad \mathbf{x} \in \Omega_P, \tag{10.1}$$
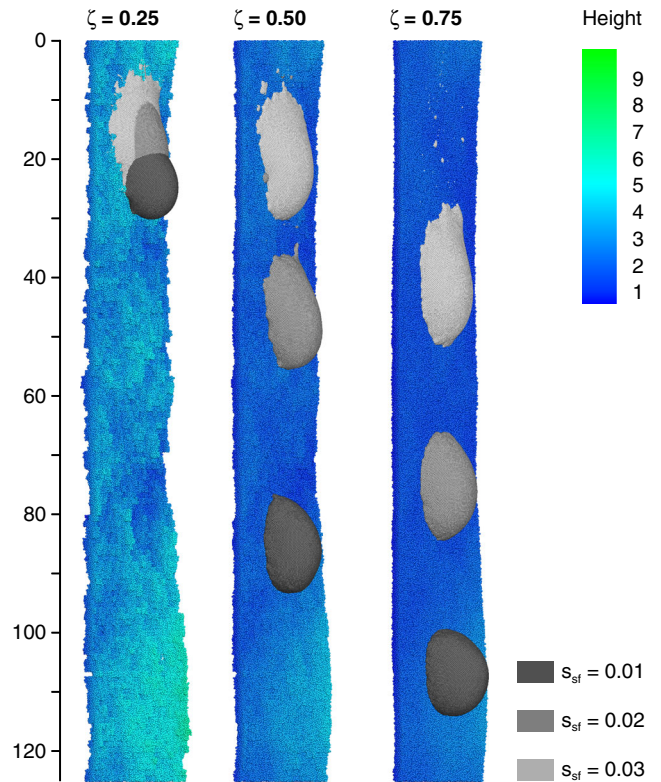
Fig. 17 Advancing droplets on rough surfaces with Hurst coefficients $\zeta = 0.25$, 0.5, and 0.75 at time $t = 2000$ (0.13 s). Results are shown for droplets with $\mu_{sph} = 0.03$ and the solid-fluid interaction strength of $s_{sf} = 0.01$, 0.02, and 0.03. The equilibrium radius of the droplets is $R_{eq} = 5.85$

subject to an appropriate initial condition and the Robin boundary condition

$$D^m\mathbf{n} \cdot \nabla C^m = g^m\left(C^1, ..., C^M, \Xi^1, ..., \Xi^L\right),$$
$$m = 1, ..., M \quad \mathbf{x} \in \Gamma. \tag{10.2}$$

Here, C^m is the mass fraction of species m, D^m is the composition dependent diffusion coefficient, r^m and g^m are the rates of the homogeneous and heterogeneous reactions of species m, respectively. $\Xi^l = S^l/S^l_{max}$ $(l = 1, ..., L)$ is the dimensionless surface concentration of species l formed on the surface (S^l_{max} is the maximum concentration). The reaction rate G^l of Ξ^l is given by:
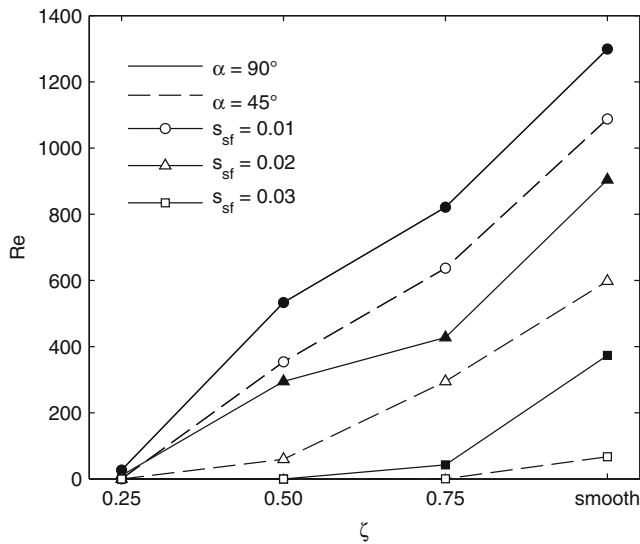
$$\frac{D\Xi^l}{Dt} = G^l\left(C^1, ..., C^M, \Xi^1, ..., \Xi^L\right),$$
$$l = 1, ..., L \quad \mathbf{x} \in \Gamma. \tag{10.3}$$

The interface Γ evolves due to precipitation/accumulation of surface species with the normal velocity v_n,

$$v_n = \sum_{l=1}^{L} \frac{S^l_{max}}{\rho^l}g^l \quad \mathbf{x} \in \Gamma. \tag{10.4}$$

Fig. 18 Reynolds numbers for three roughness coefficients, three static contact angles (110, 80, and 60°), and two inclination angles

In Section 6.2, we mentioned that a direct implementation of the Robin boundary condition in SPH can be difficult and introduced the continuum boundary force method for the Navier-Stokes equations subject to the Robin country conditions. A similar approach, the continuum surface reaction (CSR) method, has been proposed for solving advection-diffusion-reaction equations subject to Robin boundary conditions using SPH. The CSR method approximates Eqs. 10.1 and 10.2 with an advection-diffusion-reaction equation subject to the homogeneous Neumann boundary condition [61–63]:

$$\frac{DC^m}{Dt} = \frac{1}{\rho}\nabla \cdot (\rho D^m \nabla C^m) + \frac{1}{\rho}r^m\left(C^1, ..., C^M\right) + R^m,$$
$$m = 1, M \qquad (10.5)$$

and

$$D^m\mathbf{n} \cdot \nabla C^m = 0, \quad m = 1, ..., M \quad \mathbf{x} \in \Gamma. \qquad (10.6)$$

As in the CBF method, the source term R^m is related to the surface reaction g^m as:

$$R^m(\mathbf{x}) = \int_{\Omega_S} g^m(\mathbf{x}, \mathbf{y}, t)[n(\mathbf{x}) + n(\mathbf{y})]$$
$$[\psi(\mathbf{x}) - \psi(\mathbf{y})]\nabla W(\mathbf{x} - \mathbf{y}, h)d\mathbf{y} \quad \mathbf{x} \in \Omega, \quad (10.7)$$

where the computational domain is extended to $\Omega = \Omega_P \cup \Omega_S$, the color function ψ is given by Eq. 6.11 and

$$g^m(\mathbf{x}, \mathbf{y}, t) = g^m\left(C^1(\mathbf{x}), ..., C^M(\mathbf{x}), \Xi^1(\mathbf{y}), ..., \Xi^L(\mathbf{y})\right). \qquad (10.8)$$

In the CSR formulation, Ξ is found as:

$$\frac{D\Xi^l(\mathbf{x})}{Dt} = \frac{\int_\Omega G^l(\mathbf{x}, \mathbf{y}, t)[n(\mathbf{x}) + n(\mathbf{y})][\psi(\mathbf{x}) - \psi(\mathbf{y})]\nabla W(\mathbf{x} - \mathbf{y}, h)d\mathbf{y}}{\int_\Omega[n(\mathbf{x}) + n(\mathbf{y})][\psi(\mathbf{x}) - \psi(\mathbf{y})]\nabla W(\mathbf{x} - \mathbf{y}, h)d\mathbf{y}}$$
$$\mathbf{x} \in \Omega_S, \qquad (10.9)$$

where

$$G^l(\mathbf{x}, \mathbf{y}, t) = G^l\left(C^1(\mathbf{x}), ..., C^M(\mathbf{x}), \Xi^1(\mathbf{y}), ..., \Xi^L(\mathbf{y})\right). \qquad (10.10)$$

As in the PF-SPH and CBF-SPH models, the fluid and solid domains Ω_P and Ω_S are discretized with "fluid" and "solid" particles, respectively. The SPH discretization of Eq. 10.5 subject to the boundary condition (10.6) is given by

$$\frac{Dm_iC_i^m}{Dt} = \sum_{j\in\Omega_P} \frac{\left(D_i^m m_i n_i + D_j^m m_j n_j\right)\left(C_i^m - C_j^m\right)}{n_i n_j}\frac{\mathbf{r}_{ij}}{r_{ij}^2}$$
$$\cdot \nabla W(r_{ij}, h)$$
$$- m_i\sum_{j\in\Omega_S}\frac{1}{n_j}g^m\left(C_i^1, .., C_i^M, \Xi_j^1, ..., \Xi_j^L\right)[\mathbf{n}_i + \mathbf{n}_j]$$
$$\cdot \nabla W(r_{ij}, h) \quad \mathbf{r}_i \in \Omega_P \qquad (10.11)$$

and

$$\frac{D\Xi_i^l}{Dt} = \frac{\sum_{j\in\Omega_P}\frac{1}{n_j}G^l\left(C_j^1, .., C_j^M, \Xi_i^1, ..., \Xi_i^L\right)[\mathbf{n}_i + \mathbf{n}_j]\cdot\nabla W(r_{ij}, h)}{\sum_{j\in\Omega_P}\frac{1}{n_j}[\mathbf{n}_i + \mathbf{n}_j]\cdot\nabla W(r_{ij}, h)}$$
$$\mathbf{r}_i \in \Omega_S, \qquad (10.12)$$

where $\sum_{j\in\Omega_P}$ and $\sum_{j\in\Omega_S}$ denote summation over all "fluid" and "solid" particles, respectively, and the equality $\psi_i - \psi_j = 1$ for $\mathbf{r}_i \in \Omega_S$ and $\mathbf{r}_j \in \Omega_P$ is used. The last term in Eq. 10.11 is obtained by substituting Eq. 10.8 into Eq. 10.7, and discretizing the resulting integral as a Riemann sum. The SPH expression for the normal vector is given by Eq. 6.10.

It can be shown that in the limit $h \to 0$, the solution of the CSR advection-diffusion-reaction Eq. 10.5–10.10 converges to the solution of the original advection-diffusion-reaction equation subject to the Robin boundary condition. The convergence of the SPH solution of the CSR advection-diffusion-reaction equation with respect to h was demonstrated in [61, 63, 70]. The first term in Eq. 10.11 is the discretization of the diffusion term in Eq. 10.5. Summation in this term over only fluid particles enforces the homogeneous Neumann boundary condition. Dirichlet boundary condition $C^l(\mathbf{x}) = C_0$ can be imposed by setting $g^l = k\left(C^l - C_0\right)$ with sufficiently large k, but a more efficient way to prescribe the Dirichlet boundary condition is to

define artificial mass fraction C_i for the solid particles, and set $C_i = C_0$. Then, the Dirichlet boundary condition can be recovered by simply including the solid particles in summation in the diffusion term in Eq. 10.11.

The CSF model has been used to model competitive non-linear adsorption [62, 63] and growth of thin biofilms in porous media [71]. During adsorption and the type of microbial growth considered in [71], the reactive surfaces were treated as immobile, i.e., v_n was assumed to be zero.

The SPH model can be easily extended to model reactive processes leading to changes in pore geometry, including mineral precipitation and dissolution and biofilm growth. For example, for the transport of species A and B, undergoing heterogeneous reaction $A + B \rightarrow C_s$ resulting in formation of a solid phase C with the reaction rate

$$g^A = g^B = K \left(\frac{c^A c^B}{K_{sp}} - 1 \right), \tag{10.13}$$

the SPH advection-diffusion-reaction equation takes the form

$$\frac{Dm_i c_i^l}{Dt} = \sum_{j \in \Omega_P} \frac{D^I (m_i n_i + m_j n_j)\left(c_i^l - c_j^l\right)}{n_i n_j (\mathbf{r}_i - \mathbf{r}_j)^2} (\mathbf{r}_i - r_j) \cdot \nabla W (r_{ij}, h)$$
$$- m_i K \left(\frac{c_i^A c_i^B}{K_{sp}} - 1 \right) \sum_{k \in \Omega_S} \frac{2(\mathbf{n}_i + \mathbf{n}_j)}{n_i + n_j} \cdot \nabla W (r_{ij}, h), \qquad l = A, B. \tag{10.14}$$

Precipitation and dissolution of C can be modeled by tracking the masses, m_i, of the solid particles, which change according to:

$$\frac{dm_i}{dt} = -m_0 \left(C^{A,0} + C^{B,0} \right) K \sum_{j \in \Omega_P} \left(\frac{c_j^A c_j^B}{K_{sp}} - 1 \right)$$
$$\frac{2(\mathbf{n}_i + \mathbf{n}_j)}{n_i + n_j} \nabla_i W (\mathbf{r}_i - \mathbf{r}_j, h), \quad i \in s, \tag{10.15}$$

where K is the reaction rate constant, K_{sp} is the solubility product, and m_0 is the mass of solvent carried by each fluid particle. Here, c^A and c^B are normalized mass fractions of solutes A and B,

$$c^l = \frac{C^l}{C^{l,0}} \quad l = A, B, \tag{10.16}$$

C^I is the mass fraction (mass of solute I per mass of solution), and $C^{I,0}$ is the initial mass fraction. The initial mass of the solid particles is set to $m_{max} = \rho_s / n_0$, the maximum mass of C that can be contained in the volume $1/n_0$. Once m_i exceeds $2m_{max}$, its mass is reset to $m_i - m_{max}$, and a new solid particle with the mass of C equal to m_{max} is formed. A number of ways to determine the new solid particle's position can be devised. The simplest is to locate a fluid particle closest to the solid particle i and replace
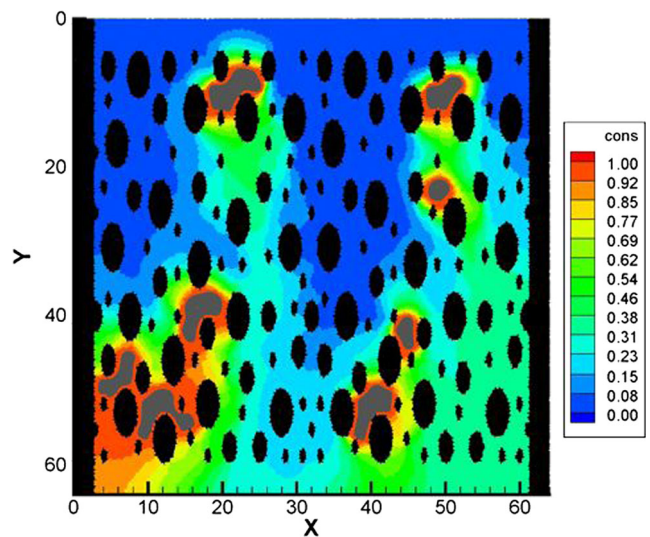
Fig. 19 The color scale represents the concentration profile, C/Ceq, of dissolved DNAPL. Gray particles represent trapped DNAPL and black particles represent soil grains and impermeable boundaries. (After [74])

it with a solid particle. Dissolution is modeled by replacing solid particles with mass equal to (or less than) zero with fluid particles. Velocity of a newly formed fluid particle can be determined using the SPH interpolation scheme $v_i = \sum_{j \in f+s} \frac{v_j}{n_j} W(r_{ij}, h)$, and the concentrations are set to $C_j^A = C_j^B = \sqrt{K_{sp}}$. A similar SPH formulation has been used in [2, 42, 72] to model precipitation of calcium carbonate as a result of mixing of calcium chloride and sodium carbonate and in [73] to model biomass growth. In the latter work, the double Monod kinetics model was used to describe the rate of biomass growth, and the biomass was treated as a viscous Newtonian fluid.

In [74], the multiphase PF-SPH model was used to solve a system of two-phase NS equations coupled with an advection-diffusion-reaction equation to model dissolution and re-immobilization of trapped non-aqueous liquid phase (NAPL), (see Fig. 19). In this work, the dissolution reaction $g = \mathcal{R}(C - C_{eq})$ was assumed, where C is the concentration of dissolved NAPL, C_{eq} is the equilibrium concentration, and $\mathcal{R}$ is the exchange rate constant.

11 Summary and prospects for future

Smoothed particle hydrodynamics (SPH) has a number of advantages for modeling complex transport processes at the pore scale. With different fluid phases modeled by different types of particles, treatment of interfacial problems is trivial in SPH compared to grid-based methods. The PF-SPH multiphase model is parameterized using surface tensions and static contact angle only, i.e., there is no need

to prescribe the dynamic receding and advancing contact angles. The dynamic contact angles are the outcome of the model and consequence of the interactions between the pairwise forces and hydrodynamic forces (viscous forces and forces produced by the pressure gradient) acting on the SPH particles near the fluid-fluid-solid interface. Advection-diffusion-reaction equations in the Lagrangian framework are reduced to diffusion-reaction equations (the solute is advected by SPH fluid particles), and there is no numerical diffusion due to discretization of the advection term.

In general, the SPH method is computationally more expensive than grid-based methods (e.g., the finite element and finite volume methods) as more neighboring particles are involved in the discretization of spatial derivatives in SPH than grid points in grid-based methods. Grid-based methods may also employ higher-order spatial discretization schemes than SPH, which uses second-order in h (the support of the weighting function) discretizations of first and second spatial derivatives. Therefore, for simple linear problems, e.g., single-phase flow, the SPH method cannot compete with grid-based methods in both accuracy and computational efficiency. On the other hand, for multiphase flow and reactive transport problems, the SPH method may provide an attractive alternative to grid-based methods. Lattice Boltzmann (LB) is another popular method for pore-scale flow simulations, which has been shown to have a smaller computational cost than the SPH method for linear single-phase flow [75]. To our knowledge, there are no rigorous comparisons of the computational costs of the LB and SPH methods for multiphase flow and reactive transport problems.

The accuracy of the SPH method can be increased by using adaptive resolution (splitting and coalescence of SPH particles) and consistent discretization of spatial derivatives. Initial work in these areas has been done for single phase Navier-Stokes equations and needs to be extended for multiphase flow and advection-diffusion-reaction equations. The computational efficiency of the SPH method can be increased by using incompressible instead of compressible SPH formulations. Incompressible SPH formulations have been used to model both single-phase and two-phase flows but mostly for problems with relatively small number of particles. The number of particles in three-dimensional pore-scale simulations could be on the order of tens of millions. Since the incompressible SPH method requires solving a Poison equation for pressure, its application for problems with a large number of particles would require efficient and scalable solvers for the resulting large systems of algebraic equations.

Methods for implementing boundary conditions remain an active research area. For example, Takeda-Morris type approaches of assigning fictitious velocities to "solid" SPH particles are second-order in h (the support of the weighting function) but can be difficult to implement for complex boundaries with sharp corners. The boundary particle method of Monaghan [76] requires some calibration and may produce pressure fluctuations near the boundaries. Diffuse-boundary type approaches, such as the continuum boundary force (CBF) and continuum surface reaction (CSR) methods, have been shown to be robust. But as immersed boundary method for a grid-based finite volume discretization of the Navier-Stokes equations [77], the CBF, and CSR methods are only first-order accurate.

Finally, we would like to mention that there are several highly scalable parallel open-source SPH codes, including GPUSPH [78], DualSPHysics [50], and GADGET [79]. These codes can be run on hardware ranging from a laptop to many core high performance computers and allow users to handle problems of various complexity with little additional code development.

References

1. Tartakovsky, A.M., Ward, A.L., Meakin, P.: Pore-scale simulations of drainage of heterogeneous and anisotropic porous media. Phys. Fluids **19**(10), 103301 (2007)

2. Tartakovsky, A.M., Redden, G., Lichtner, P., Scheibe, T., Meakin, P.: Mixing-induced precipitation: experimental study and multiscale numerical analysis. Water Resour. Res. **44**, W06S04 (2008)

3. Battiato, I., Tartakovsky, D.M., Tartakovsky, A.M., Scheibe, T.D.: Hybrid models of reactive transport in porous and fractured media. Adv. Water Resour. **34**(9), 1140–1150 (2011)

4. Tartakovsky, A., Scheibe, T.: Dimension reduction numerical closure method for advection-diffusion-reaction systems. Adv. Water Resour. **34**(12), 1616–1626 (2011)

5. de Anna, P., Borgne, T.L., Dentz, M., Tartakovsky, A.M., Bolster, D., Davy, P.: Flow intermittency, dispersion, and correlated continuous time random walks in porous media. Phys. Rev. Lett. **110**(18), 184502 (2013)

6. Tartakovsky, A.M.: Langevin model for reactive transport in porous media. Phys. Rev. E. **82**(2), 026302 (2010)

7. Ovaysi, S., Piri, M.: Direct pore-level modeling of incompressible fluid flow in porous media. J. Comput. Phys. **229**(19), 7456–7476 (2010)

8. Meakin, P., Tartakovsky, A.M.: Modeling and simulation of pore scale multiphase fluid flow and reactive transport in fractured and porous media. Rev. Geophys. **47**, RG3002 (2009)

9. Monaghan, J.J.: Smoothed particle hydrodynamics. Rep. Prog. Phys. **68**(8), 1703 (2005)

10. Antuono, M., Colagrossi, A., Marrone, S., Molteni, D.: Free-surface flows solved by means of SPH schemes with numerical diffusive terms. Comput. Phys. Commun. **181**(3), 532–549 (2010)

11. Pan, W., Tartakovsky, A., Monaghan, J.: Smoothed particle hydrodynamics non-newtonian model for ice-sheet and ice-shelf dynamics. J. Comput. Phys. **242**(0), 828–842 (2013)

12. Monaghan, J.: Smoothed particle hydrodynamics and its diverse applications. Ann. Rev. Fluid Mech. **44**, 323–346 (2012)

13. Tanner, L.H.: The spreading of silicone oil drops on horizontal surfaces. J. Phys. D: Appl. Phys. Email Alert RSS Feed **12**(9), 1473 (1979)

14. de Gennes, P.: Wetting: statics and dynamics. Rev. Mod. Phys. **57**(3), 827–863 (1985)

15. Dussan V, E.: On the spreading of liquids on solid surfaces: static and dynamic contact lines. Annu. Rev. Fluid Dyn. **11**, 371–400 (1979)

16. Huh, C., Scriven, L.: Hydrodynamic model of steady movement of a solid/liquid/fluid contact line. J. Colloid Interface Sci. **35**(1), 85–101 (1971)

17. Tartakovsky, A.M., Meakin, P.: Pore scale modeling of immiscible and miscible fluid flows using smoothed particle hydrodynamics. Adv. Water Resour. **29**(10), 1464–1478 (2006)

18. Quinlan, N.J., Basa, M., Lastiwka, M.: Truncation error in mesh-free particle methods. Int. J. Numer. Methods Eng. **66**(13), 2064–2085 (2006)

19. Brackbill, J., Kothe, D.B., Zemach, C.: A continuum method for modeling surface tension. J. Comput. Phys. **100**(2), 335–354 (1992)

20. Kordilla, J., Tartakovsky, A., Geyer, T.: A smoothed particle hydrodynamics model for droplet and film flow on smooth and rough fracture surfaces. Adv. Water Resour. **59**(0), 1–14 (2013)

21. Zhou, G., Ge, W., Li, J.: A revised surface tension model for macro-scale particle methods. Powder Technol. **183**(1), 21–26 (2008)

22. Nugent, S., Posch, H.: Liquid drops and surface tension with smoothed particle applied mechanics. Phys. Rev. E **62**(4), 4968 (2000)

23. Meleán, Y., Sigalotti, L.D.G., Hasmy, A.: On the SPH tensile instability in forming viscous liquid drops. Comput. Phys. Commun. **157**(3), 191–200 (2004)

24. Meleán, Y., Sigalotti, L.D.G.: Coalescence of colliding van der Waals liquid drops. Int. J. Heat Mass Transfer **48**(19), 4041–4061 (2005)

25. Bandara, U., Tartakovsky, A., Oostrom, M., Palmer, B., Grate, J., Zhang, C.: Smoothed particle hydrodynamics pore-scale simulations of unstable immiscible flow in porous media, Advances in Water Resources 62, Part C (0) (2013) 356–369

26. Young, T.: An essay on the cohesion of fluids. Philos. Trans. R. Soc. Lond. **95**, 65–87 (1805)

27. Maxwell, J.: The Scientific Papers of J.M. Maxwell, Capillary Actions, vol. 2, p. 541. Cambridge University Press (1890)

28. Rayleigh, L.: On the theory of surface forces. In: Collected Papers, vol. 3, Art. 176, pp. 397–425. Dover, New York (1964)

29. Morris, J.P.: Simulating surface tension with smoothed particle hydrodynamics. Int. J. Numer. Methods Fluids **33**(3), 333–353 (2000)

30. Hu, X., Adams, N.: A multi-phase SPH method for macroscopic and mesoscopic flows. J. Comput. Phys. **213**(2), 844–861 (2006)

31. Graham, D.I., Hughes, J.P.: Accuracy of SPH viscous flow models. Int. J. Numer. Methods Fluids **56**(8), 1261–1269 (2008)

32. Basa, M., Quinlan, N.J., Lastiwka, M.: Robustness and accuracy of SPH formulations for viscous flow. Int. J. Numer. Methods Fluids **60**(10), 1127–1148 (2009)

33. Fatehi, R., Manzari, M.: Error estimation in smoothed particle hydrodynamics and a new scheme for second derivatives. Comput. Math. Appl. **61**(2), 482–498 (2011)

34. Hashemi, M., Fatehi, R., Manzari, M.: A modified SPH method for simulating motion of rigid bodies in Newtonian fluid flows. Int. J. Non-Linear Mech. **47**(6), 626–638 (2012)

35. Chorin, A.J.: A numerical method for solving incompressible viscous flow problems. J. Comput. Phys. **2**(1), 12–26 (1967)

36. Tamamidis, P., Zhang, G., Assanis, D.N.: Comparison of pressure-based and artificial compressibility methods for solving 3d steady incompressible viscous flows. J. Comput. Phys. **124**(1), 1–13 (1996)

37. Morris, J.P., Fox, P.J., Zhu, Y.: Modeling low Reynolds number incompressible flows using SPH. J. Comput. Phys. **136**(1), 214–226 (1997)

38. Monaghan, J.J.: Simulating free surface flows with SPH. J. Comput. Phys. **110**(2), 399–406 (1994)

39. Lastiwka, M., Basa, M., Quinlan, N.J.: Permeable and non-reflecting boundary conditions in SPH. Int. J. Numer. Methods Fluids **61**(7), 709–724 (2009)

40. Swegle, J., Hicks, D., Attaway, S.: Smoothed particle hydrodynamics stability analysis. J. Comput. Phys. **116**(1), 123–134 (1995)

41. Balsara, D.S.: Von Neumann stability analysis of smoothed particle hydrodynamics—suggestions for optimal algorithms. J. Comput. Phys. **121**(2), 357–372 (1995)

42. Tartakovsky, A.M., Meakin, P., Scheibe, T.D., Eichler West, R.M.: Simulations of reactive transport and precipitation with smoothed particle hydrodynamics. J. Comput. Phys. **222**(2), 654–672 (2007)

43. Holmes, D.W., Williams, J.R., Tilke, P.: Smooth particle hydrodynamics simulations of low Reynolds number flows through porous media. Int. J. Numer. Anal. Methods Geomech. **35**(4), 419–437 (2011)

44. Cummins, S.J., Rudman, M.: An SPH projection method. J. Comput. Phys. **152**(2), 584–607 (1999)

45. Lee, E.-S., Moulinec, C., Xu, R., Violeau, D., Laurence, D., Stansby, P.: Comparisons of weakly compressible and truly incompressible algorithms for the SPH mesh free particle method. J. Comput. Phys. **227**(18), 8417–8436 (2008)

46. Xu, R., Stansby, P., Laurence, D.: Accuracy and stability in incompressible SPH (ISPH) based on the projection method and a new approach. J. Comput. Phys. **228**(18), 6703–6725 (2009)

47. Hosseini, S.M., Feng, J.J.: Pressure boundary conditions for computing incompressible flows with SPH. J. Comput. Phys. **230**(19), 7473–7487 (2011)

48. Litvinov, S., Ellero, M., Hu, X., Adams, N.: A splitting scheme for highly dissipative smoothed particle dynamics. J. Comput. Phys. **229**(15), 5457–5464 (2010)

49. Trask, N., Maxey, M., Kim, K., Perego, M., Parks, M.L., Yang, K., Xu, J.: A scalable consistent second-order SPH solver for unsteady low reynolds number flows. Computer Methods in Applied Mechanics and Engineering. doi:10.1016/j.cma.2014.12.027

50. Domínguez, J.M., Crespo, A.J., Valdez-Balderas, D., Rogers, B., Gómez-Gesteira, M.: New multi-GPU implementation for smoothed particle hydrodynamics on heterogeneous clusters, Computer Physics Communications

51. Tartakovsky, A., Meakin, P.: Modeling of surface tension and contact angles with smoothed particle hydrodynamics. Phys. Rev. E **72**(2), 026301 (2005)

52. Tartakovsky, A.M., Meakin, P.: Simulation of free-surface flow and injection of fluids into fracture apertures using smoothed particle hydrodynamics. Vadose Zone J. **4**(3), 848–855 (2005)

53. Allen, M.P., Tildesley, D.J.: Computer simulation of liquids. Oxford university press (1989)

54. Monaghan, J.: Simulating free surface flows with SPH. J. Comput. Phys. **110**(2), 399–406 (1994)

55. Gomez-Gesteira, M., Rogers, B.D., Crespo, A.J.C., Dalrymple, R.A., Narayanaswamy, M., Dominguez, J.M.: SPHysics

- development of a free-surface fluid solver—part 1: Theory and formulations. Comput. Geosci. **48**, 289–299 (2012). doi:10.1016/j.cageo.2012.02.029

56. Liu, G.R., Liu, M.B.: Smoothed particle hydrodynamics: a mesh-free particle method. World Scientific Publishing (2003)

57. Monaghan, J.J.: SPH without a tensile instability. J. Comput. Phys. **159**(2), 290–311 (2000)

58. Maciá, F., Antuono, M., González, L.M., Colagrossi, A.: Theoretical analysis of the no-slip boundary condition enforcement in SPH methods. Prog. Theor. Phys. **125**(6), 1091–1121 (2011)

59. Takeda, H., Miyama, S.M., Sekiya, M.: Numerical simulation of viscous flow by smoothed particle hydrodynamics. Prog. Theor. Phys. **92**(5), 939–960 (1994)

60. Pan, W., Bao, J., Tartakovsky, A.M.: Smoothed particle hydrodynamics continuous boundary force method for Navier-Stokes equations subject to a Robin boundary condition. J. Comput. Phys. **259**(0), 242–259 (2014)

61. Ryan, E.M., Tartakovsky, A.M., Amon, C.: A novel method for modeling Neumann and Robin boundary conditions in smoothed particle hydrodynamics. Comput. Phys. Commun. **181**(12), 2008–2023 (2010)

62. Ryan, E., Tartakovsky, A., Recknagle, K., Khaleel, M., Amon, C.: Pore-scale modeling of the reactive transport of chromium in the cathode of a solid oxide fuel cell. J. Power Sources **196**(1), 287–300 (2011)

63. Ryan, E.M., Tartakovsky, A.M., Amon, C.: Pore-scale modeling of competitive adsorption in porous media. J. Contam. Hydrol. **120-121**(0), 56–78 (2011)

64. Bocquet, L., Barrat, J.-L.: Flow boundary conditions from nano-to micro-scales. Soft Matter **3**(6), 685–693 (2007)

65. Peskin, C.S.: The immersed boundary method. Acta numerica **11**, 479–517 (2002)

66. Li, X., Lowengrub, J., Rätz, A., Voigt, A.: Solving PDEs in complex geometries: a diffuse domain approach. Commun. Math. Sci. **7**(1), 81 (2009)

67. Pereira, G., Prakash, M., Cleary, P.: SPH modelling of fluid at the grain level in a porous medium. Appl. Math. Model. **35**(4), 1666–1675 (2011)

68. Zhang, C., Oostrom, M., Wietsma, T.W., Grate, J.W., Warner, M.G.: Influence of viscous and capillary forces on immiscible fluid displacement: Pore-scale experimental study in a water-wet micromodel demonstrating viscous and capillary fingering. Energy and Fuels **25**(8), 3493–3505 (2011)

69. Gouet-Kaplan, M., Tartakovsky, A.M., Berkowitz, B.: Interplay of resident and infiltrating water. Water Resour. Res. **45**, W05416 (2009)

70. Du, Q., Lehoucq, R., Tartakovsky, A.: Integral approximations to classical diffusion and smoothed particle hydrodynamics. Comput. Methods Appl. Mech. Eng. **286**, 216–229 (2015). http://www.sciencedirect.com/science/article/pii/S0045782514004988

71. Tartakovsky, G., Tartakovsky, A., Scheibe, T., Fang, Y., Mahadevan, R., Lovley, D.: Pore-scale simulation of microbial growth using a genome-scale metabolic model: implications for darcy-scale reactive transport. Adv. Water Resour. **59**, 256–270 (2013)

72. Tartakovsky, A.M., Meakin, P., Scheibe, T., Wood, B.: A smoothed particle hydrodynamics model for reactive transport and mineral precipitation in porous and fractured porous media. Water Resour. Res. **43**, W05437 (2007)

73. Tartakovsky, A.M., Scheibe, T.D., Meakin, P.: Pore-scale model for reactive transport and biomass growth. J. Porous Media **12**(5), 417–434 (2009)

74. Tartakovsky, A., Meakin, P., Ward, A.: Smoothed particle hydrodynamics model of non-aqueous phase liquid flow and dissolution. Transp. Porous Media **76**, 11–34 (2009)

75. Pereira, G.G., Dupuy, P.M., Cleary, P.W., Delaney, G.W.: Comparison of permeability of model porous media between SPH and LB. Progress in Computational Fluid Dynamics, an International Journal **12**(2), 176–186 (2012)

76. Monaghan, J., Kajtar, J.: Sph particle boundary forces for arbitrary boundaries. Comput. Phys. Commun. **180**(10), 1811–1820 (2009)

77. Peskin, C.S., McQueen, D.M.: A three-dimensional computational method for blood flow in the heart i. immersed elastic fibers in a viscous incompressible fluid. J. Comput. Phys. **81**(2), 372–405 (1989)

78. Hérault, A., Bilotta, G., Dalrymple, R.A.: SPH on gpu with cuda. J. Hydraul. Res. **48**(S1), 74–79 (2010)

79. Springel, V., Yoshida, N., White, S.D.: GADGET: a code for collisionless and gasdynamical cosmological simulations. New Astron. **6**(2), 79–117 (2001)